

Wall Temperature and Rotation Rate Effects on the Magnus Force of a Spinning Rocket

XUE, Kuiju, ZHAO, Liangyu, LI, Qinling <<http://orcid.org/0000-0002-7191-9538>> and JIAO, Longyin

Available from Sheffield Hallam University Research Archive (SHURA) at:

<https://shura.shu.ac.uk/28087/>

This document is the Accepted Version [AM]

Citation:

XUE, Kuiju, ZHAO, Liangyu, LI, Qinling and JIAO, Longyin (2021). Wall Temperature and Rotation Rate Effects on the Magnus Force of a Spinning Rocket. Heat Transfer Engineering. [Article]

Copyright and re-use policy

See <http://shura.shu.ac.uk/information.html>

Wall Temperature and Rotation Rate Effects on the Magnus Force of a Spinning Rocket

Kuiju Xue^a, Liangyu Zhao^{a*}, Qinling Li^b and Longyin Jiao^a

^a*School of Aerospace Engineering, Beijing Institute of Technology, Beijing 100081, P. R. China*

^b*Department of Engineering and Mathematics/MERI, Sheffield Hallam University, Sheffield, S1*

1WB, UK

Abstract

The current work focuses on wall temperature (300 - 1200 K), dimensionless spin rate (0 - 0.315) and angles of attack (0 - 10°) on Magnus effects for the 7-caliber Army-Navy Spinner Rocket (ANSR) using Reynolds-averaged Navier-Stokes methods. The Mach number and the Reynolds number, in terms of the free-stream velocity and the ANSR diameter, are 1.8 and 8.37×10^5 . Different turbulence models are verified by a fully developed turbulent channel flow to ensure accurate prediction of the near-wall turbulence. The k -epsilon Yang-Shih model provides a favorable result in terms of the logarithmic velocity, turbulent kinetic energy, turbulent shear stress and dissipate rate. The ANSR simulations suggest that the Magnus force is approximately proportional to the dimensionless spin rate. Furthermore, the simulations provide a profound insight into the flow structure and reveal that the separation point moves forward with the increasing dimensionless spin rate. With the increase of angle of attack between 0 - 10°, the boundary layer thickness distortion increases, however the variation of the separation point is

negligible. The current study also suggests that higher surface temperature has a positive effect on reducing the Magnus and drag forces, in the meantime, on increasing the lift force.

*Address correspondence to Associate Professor Liangyu Zhao, School of Aerospace Engineering, Beijing Institute of Technology, 5 South Zhongguancun Street, 100081 Beijing, P. R. China. E-mail: zhaoly@bit.edu.cn.

Introduction

Spinning rockets have advantages in simplifying control systems and reducing costs, so they have received widespread attention. However, the spinning rockets have a unique aerodynamic characteristic, the Magnus effect. The Magnus effect of the spinning rocket is a phenomenon in which a lateral force is generated in a direction perpendicular to the plane formed by the rotational angular velocity vector and the velocity vector when the rotational angular velocity vector does not coincide with the centroid motion velocity vector. It has an important impact on flight trajectory and dynamic stability. In severe cases, it will cause divergent conical motion. Researches have been carried out to further understand the Magnus mechanism, in order to better predict and control the Magnus effect of spinning rockets. However, the work in this field is still very limited.

The magnitude of the Magnus effect depends on multiple parameters including the spin rate, wall temperature, angle of attack (AOA), fineness, Mach number and Reynolds number. Any change in these parameters will lead to a different state of the boundary layer condition, hence affect the Magnus effect, flight trajectory and dynamic stability.

Prior experimental studies, both on free-flying [1 - 3] as well as wind tunnel mounted projectiles [4, 5], and computational fluid dynamics (CFD) simulations [2, 5 - 7] using Reynolds-averaged Navier-Stokes (RANS) method provide some useful database for Magnus forces and moments. In experiments, Murphy & Schmidt [1], Schmidt & Murphy [2], Donneaud et al. [3], Luchuk & Sparks [4] and Klatt & Hruschka [5] studied the Magnus effect of spinning rockets at different angles of attack. Luchuk & Sparks [4] experimental results show that for a 7-diameter long rocket with a 2-diameter long nose the maximum Magnus lateral force coefficient appears in the range of 10° to 15° . Although experiments are normally considered the most reliable means to

obtain accurate aerodynamic parameters, including Magnus force, there are certain shortcomings: wind tunnel experiments are often limited in the range of accessible flow conditions, especially at low Reynolds numbers, which leads to a different boundary layer state where the transition from laminar to turbulent flow occurs somewhere along the body. This, in turn, leads to nonlinear dependencies of the Magnus force on parametric studies, such as AOA and spin rate, etc. Furthermore, experiments are expensive, and the visibility of the flow structure is limited. There are certain deficiencies in analysing the flow structures to reveal the flow mechanisms. In CFD simulations, Pechier et al. [8] and Siltou [9] numerically simulated the flow field around a spinning rocket at transonic and supersonic speeds. DeSpirio and co-workers [10 - 12] simulated the impact of the stern of the rotating projectile on Magnus force using CFD ++, and found that the geometry of the tail of the projectile has a significant influence on the magnitude of the Magnus force. The numerical work of the predecessors mainly focused on the studies of the Magnus effect with different AOA, the geometry of the tail, Reynolds number and Mach number. There are few articles on the effects of wall temperature and dimensionless spin rate variations on the Magnus effects. In addition, although the previous simulation values of the drag coefficient and lift coefficient are in good agreement with the experiments and semi-empirical formulae, there is still a certain deviation from the experimental values in the prediction of Magnus force and Magnus moments, which motivate the current work.

The present investigation concentrates on improving the accuracy of predicting the Magnus effect of the spinning rocket and incorporating the wall temperature into the factors that affect the Magnus effect, which extends the work of the predecessors. In order to predict the Magnus force more accurately, different turbulence models have been verified by a fully developed turbulent channel flow [13 - 17] firstly. The fully developed turbulent channel flow simulation has the

advantages of simple geometric shape and easy formation of high-quality orthogonal mesh, and the simulation results can be compared with those from direct numerical simulation (DNS) [16]. Based on the fully developed turbulent channel flow benchmark results, the three-dimensional RANS equation and k-ε Yang-Shih model [17 - 20] in ANSYS Fluent 18.2 are employed to simulate the Magnus effect for the 7-caliber ANSR of different dimensionless rotational angular velocities, different angles of attack and different wall temperatures. The simulation results are visualized to further study the effect of each parameter on the Magnus effect. And the simulation data are also reanalyzed using modern reduction techniques in an attempt to give some empirical formulas for Magnus force with rotational angular velocity, AOA and wall temperature, so that the Magnus effect can be predicted quickly in engineering.

Governing equations and turbulence modeling

The three-dimensional compressible Navier-Stokes governing equations of the differential form are given by

$$\begin{cases} \frac{\partial \rho}{\partial t} + \frac{\partial}{\partial x_i}(\rho u_i) = 0 \\ \frac{\partial}{\partial t}(\rho u_i) + \frac{\partial}{\partial x_j}(\rho u_i u_j) = -\frac{\partial P}{\partial x_i} + \frac{\partial}{\partial x_j}(\mu \frac{\partial u_i}{\partial x_j} - \langle \rho u_i u_j \rangle) \\ \frac{\partial \rho e}{\partial t} + \frac{\partial}{\partial x_i}(\rho e u_i) + \frac{\partial}{\partial x_i}(P u_i) + \frac{\partial q}{\partial x_i} = \frac{\partial}{\partial x_i} u_i (\mu \frac{\partial u_i}{\partial x_j} - \langle \rho u_i u_j \rangle) \end{cases} \quad (1)$$

where ρ is the density; t is the time, u_i (or u_j) is the Favre averaged velocities in x_i (x_j) direction, where $i, j = 1, 2, 3$; P is the static pressure; μ is the dynamic viscosity; e is total energy per unit volume; and q is the heat flux generated by heat conduction, and for ideal gas, $P = \rho RT$.

In an eddy viscosity model, one assumes the Reynolds stresses are related to the mean velocity field by [17]

$$-\langle \rho u_i u_j \rangle = \mu_T \left(\frac{\partial u_i}{\partial x_j} + \frac{\partial u_j}{\partial x_i} \right) - \frac{2}{3} \rho k \delta_{ij} \quad (2)$$

Where, the Kronecker delta symbol, δ_{ij} , is a piecewise function with $\delta_{ij} = 1$ if $i = j$ and 0 otherwise.

And

$$\mu_T = \rho c_\mu \frac{k^2}{\varepsilon}$$

And the transport equations for k and ε are as [18]

$$\begin{aligned} \frac{\partial(\rho k)}{\partial t} + \frac{\partial(\rho k u_j)}{\partial x_j} &= \frac{\partial}{\partial x_j} \left[\left(\mu + \frac{\mu_T}{\sigma_k} \right) \frac{\partial k}{\partial x_j} \right] - \langle \rho u_i u_j \rangle \frac{\partial u_i}{\partial x_j} - \rho \varepsilon \\ \frac{\partial(\rho \varepsilon)}{\partial t} + \frac{\partial(\rho \varepsilon u_j)}{\partial x_j} &= \frac{\partial}{\partial x_j} \left[\left(\mu + \frac{\mu_T}{\sigma_\varepsilon} \right) \frac{\partial \varepsilon}{\partial x_j} \right] - \left(-C_{1\varepsilon} \langle \rho u_i u_j \rangle \frac{\partial u_i}{\partial x_j} - \rho C_{2\varepsilon} \varepsilon \right) / T_t + \rho E \end{aligned} \quad (3)$$

Where

$$\begin{aligned} T_t &= \frac{k}{\varepsilon} + c_k \left(\frac{\mu}{\rho \varepsilon} \right)^{1/2} \\ \rho^2 E &= \mu \mu_T \frac{\partial^2 u_i}{\partial x_i \partial x_k} \frac{\partial^2 u_i}{\partial x_i \partial x_k} \end{aligned}$$

The constants $c_\mu = 0.09$, $C_{1\varepsilon} = 1.44$, $C_{2\varepsilon} = 1.92$, $\sigma_k = 1.0$, and $\sigma_\varepsilon = 1.3$. The term of E is confined to the buffer layer. The RANS equations are solved using the double precision density-based solver. A second-order upwind scheme is adopted for spatial discretization. For convective fluxes, Roe-FDS [21] flux-difference splitting scheme is utilized. Gradients are computed with the least-squares gradient method.

In the first part, different turbulence models are tested by a fully developed turbulent channel flow. As for calculating the channel flow, $i, j = 1, 2$ and the density is constant. In this way, the RANS equations are simplified into a two-dimensional incompressible format. Based on the verification, the k - ε Yang-Shih model is employed to study the three-dimensional model of ANSR in the second part.

Verification: turbulence modeling

The study, in this section, investigates the validity, accuracy, cost and applicability of several RANS turbulent models, such as the k- ϵ model with RNG and enhanced wall treatment (EWT), the k- ϵ realizable with low-Re and time scale based Yang & Shih model [18], and k- ω models (SST and BSL), by simulating the near wall characteristics of fully-developed turbulent channel flow. Due to the simplicity and the high quality of the grid, the simulation cost of the verification can be reduced while ensuring accuracy.

The simulation domain is $(1 \times 2)h$, and a full-structure grid is utilized to ensure that the channel wall resolution is sufficiently high ($y^+ \sim 0.5$). Periodic boundary condition is applied to the inlet and outlet, with pressure gradient of $dP/dx = -1$ to ensure a fully developed turbulent flow. No-slip conditions are utilized to the channel walls such that the velocity at wall is zero. The Reynolds number based on the wall friction speed is 590, which corresponds to a Reynolds number of approximately 1.2×10^4 based on the centerline velocity. Double precision coupled solver is selected. The interpolation method for pressure remains at second-order, and third-order discretization is applied to all other terms. Convergence criteria for all simulations requires residuals below 1×10^{-7} .

The comparison of the current results with those from the DNS [16] is shown in Figure 1. The results from the popular k- ϵ , RNG with EWT model, the k- ω BSL model with low-Re correction, and the low Re k- ϵ Yang-Shin model [18] are shown in this paper. Figure 1(a) illustrates the mean dimensionless streamwise velocity profile (u/u_τ) against y^+ (here, $y^+ = \rho u_\tau y / \mu$, y is the wall normal distance, and u_τ is the wall friction velocity); the dimensionless turbulent kinetic energy, $k^+ = k / u_\tau^2$, and Reynolds shear stress, $\langle -u'v' \rangle$, variations along the channel width direction, y/h , can be found in Figure 1(b) and (c). The turbulent viscosity, μ_t , is plotted in Figure 1(d). From

Figure 1, it is evident that the result with k- ϵ Yang-Shih model [18] provides better agreement with DNS than those with the other two models, especially for the peak k^+ value and the turbulent viscosity in the viscous sublayer and buffer layer, which is linked to the energy cascade rate and the turbulence structure. Note from Figure 1(d) that the k- ϵ Yang-Shih model [18] provides a wrong trend in μ_T close to the channel centerline compared with DNS and other two models, which suggests further investigation for the k- ϵ Yang-Shih model [18] implementation away from the wall, in Fluent, is necessary, as the model works well in reference [16] at $Re_\tau = 395$. However, the magnitude of the current turbulent viscosity value with the Yang-Shih model [18] is closer to the DNS compared those with the other two models in the channel centerline. Thus, the k- ϵ Yang-Shih model [18] is considered to better predict the wall-bounded flow, which will provide a basis for the work in the next section.

Simulations of the Magnus force of a spinning rocket

The study in this section investigates the impact of the different dimensionless spin rate ($\bar{p} = 0 - 0.315$), AOA ($\alpha = 0^\circ - 10^\circ$) and wall temperature ($T_w = 300 \text{ K} - 1200 \text{ K}$) on Magnus effect for the 7-caliber ANSR using the RANS approach.

Geometric models and meshing

The computational model of the ANSR is 7-diameter ($d = 20 \text{ mm}$) in total length as shown in Figure 2. It consists of a 2d secant ogive followed by a 5d cylindrical afterbody [2, 12].

A three-dimensional structured grid is generated using the ANSYS ICEM software. The overall structured mesh and the symmetry plane are shown in Figures 3 (a) and (b). The distance

between the entrance of the simulation domain and the nose cone is 35 times the diameter of the projectile. The length between the tail of the projectile and the outlet of the calculation domain is 50 times the diameter of the projectile; and the dimension in the radial direction of the projectile is 50 times the diameter of the projectile. The topology of the 3D mesh is shown in Figure 3 (c). An O-grid type mesh with a distance of $0.1d$ from the rocket body is generated to maintain a fine mesh quality required to resolve the viscous sublayer. The first-edge spacing used for this mesh is $2.5 \times 10^{-5}d$, which yields a y^+ value of 0.5 or less to ensure capturing the Magnus effect of the spinning shell. A C-grid type mesh with a stretching ratio of 1.0 is generated around the body to a distance of $0.5d$. All mesh stretching ratios are kept below 1.2; aspect ratios are between 1 and 20 and angles are greater than 45° .

Mesh independent study is performed on multiple simulations with three typical mesh densities, which are listed in Table 1. The simulation results using RANS with k- ϵ Yang-Shih model [18] of the three grids are in good agreement. The relative differences of the lateral force are less than 0.5%, as shown in Figure 4. So the Mesh1 resolution is considered to be sufficiently high. In addition, the Mesh1 case running time to achieve a convergent solution is only about one quarter of the Mesh3 one. So, in this work, Mesh1 is chosen for the parametric studies of the Magnus effect, such as different dimensionless rotational angular velocities, angles of attack and wall temperatures. Note: N_{in} is the number of nodes between the inlet and the model nose. N_l is the node number in the streamwise direction, and N_c is the node number in the circumferential direction. N_{out} is the number of nodes between the end of the model and the outlet. In the wall normal direction, N_b is the node number in the O-shaped boundary region; while N_{lr} is the node number in radial direction of the C-shaped region; the node number radial direction of outside the C-shaped region is N_{2r} .

Boundary conditions and test cases

A far-field supersonic boundary condition, with standard free stream temperature and pressure (101.325 kPa, 288 K) and Mach number of 1.8, is adopted. The Reynolds number, in terms of the free stream velocity and the ANSR diameter, is 8.37×10^5 . A non-slip isothermal and rotational wall boundary condition is employed for the rocket surface, in order to avoid the moving reference frame. All calculations are considered to converge when the residuals are below 1×10^{-7} , and the amount of change in the aerodynamic coefficient value is less than 0.1% in the last 500 steps.

Parametric studies of Magnus effects are shown in Table 2. In the first part, simulations at six dimensionless spin rate: $\bar{p} = 0, 0.05, 0.107, 0.151, 0.230$ & 0.315 , respectively, are investigated at $\alpha = 4^\circ$, $Ma = 1.8$ and $T_w = 300$ K. Here, $\bar{p} = pd/2u_\infty$, p is the spin rate and u_∞ is the freestream velocity. In the second part, simulations with six angles of attack, $\alpha = 0^\circ, 2^\circ, 4^\circ, 6^\circ, 8^\circ$ & 10° , respectively, are carried out to reveal the AOA on the Magnus effect at $Ma = 1.8$, $\bar{p} = 0.315$ & $T_w = 300$ K. In order to probe the wall temperature effect, four wall temperatures ($T_w = 300$ K, 600 K, 900 K & 1200 K, respectively) on the Magnus effect are investigated at $Ma = 1.8$, $\bar{p} = 0.315$ and $\alpha = 8^\circ$ in the third part.

Magnus effect of different AOA

In order to represent the quantitative relationship between the Magnus force and the AOA, the lateral force corresponding to different angles of attack is normalized by the dimensionless spin rate as a new dimensionless parameter C_{yp} (where, $C_{yp} = C_y/\bar{p}$). Figure 5 shows the simulated C_{yp} with different angles of attack comparing with experimental and numerical results in reference [5]. To compare the current data with those in references, the Reynolds number (Re) and the

fineness (l/d) of Klatt effect [5] have been taken into consideration. Iversen [22] suggested that C_{yp} is proportional to $Re^{-0.25}(l/d)^2$. Hence, the Klatt's experimental data [5] has been adjusted accordingly with an aspect ratio l/d of 6.37 at a Reynolds number of 1.09×10^7 using equation (4):

$$C_{yp} = C_{ypR} \left(\frac{l_{current} / d_{current}}{l_{Ref} / d_{Ref}} \right)^2 \left(\frac{Re_{Ref}}{Re_{current}} \right)^{1/4} \quad (4)$$

The fineness of the rotating rocket in Wilcox's experiment [20] is the same as that of the simulation model in this paper, which is 7. In order to approach the current simulation conditions, the Magnus force coefficient values at different angles of attack at Mach numbers of 1.77 and 2.21 were selected from the experimental results of Wilcox [20], and the Reynolds numbers were 4.7×10^5 and 3.33×10^5 respectively. Both Wilcox [20] and Klatt [5] reported in their articles that the method of eliminating systematic errors in their experiment and the repeatability of the experimental results. All data are shown in Figure 5 corrected according to equation (4). The revised experimental data of Wilcox and Klatt are relatively close, but not completely coincident. On the one hand, there may be a certain error due to different conditions. On the other hand, this also means that although equation (4) is instructive, it is not perfect. It is more meaningful to compare simulation results with experimental results with similar conditions. Therefore, for Klatt's experimental data, the error bars relative to Klatt's simulation results are marked in the figure, and the error bars relative to the current simulation results are only marked on the Wilcox's experiment data. When the AOA is less than 4° , the simulation results almost coincide with the experimental values. While when the AOA is greater than 4° , the error occasionally increases, and the maximum error is 16% at about 7° . The error of Klatt's simulation results compared to the experimental value tends to gradually expand with the increase of the AOA, and it reaches 48% at 7° . Considering that the Magnus force coefficient is usually only about one-tenth to one-twentieth of the lift coefficient and drag coefficient, which is difficult to simulate and measure, the error of the current simulation

results is acceptable. Furthermore, the current simulation result is more accurate than the numerical solution in references [5], which will support the follow-up discussions.

For a better understanding of the mechanism of AOA influence on Magnus effect, the pressure field with the superimposed cross-flow velocity streamlines for different angles of attack over the range $0^\circ - 10^\circ$ (increment of 2°) at Mach number of 1.8 and dimensionless spin rate of 0.315 are shown in Figure 6. Note that the pressure on the right side of the rotating body decreases rapidly when the AOA increases. Although the pressure on the left side decreases, the degree of reduction is significantly smaller than that on the right side, which results in an overall increase in the lateral force following the AOA increase. The vortex at the upper left of the projectile increases gradually, and the distortion of the boundary layer thickness along the circumferential direction becomes more significant. This indicates that the magnitude of the Magnus force is positively correlated with the AOA at least within the range of $0^\circ - 10^\circ$. At the same time, the position of the airflow separation point on the left side of the body is negligible ($\sim -90^\circ$), which means that distortion of the boundary layer thickness is the main factor affecting the magnitude of the Magnus force at different AOA.

The circumferential pressure distribution curve normalized by the freestream static pressure P_∞ for different AOA at $x = 4.5d$ are displayed in Figure 7. At $\alpha = 0^\circ$, the circumferential pressure distribution curve of the projectile is horizontal line, indicating that the pressure distribution is uniform. As the AOA increases, the pressure value at -120° , 40° & 90° drag curve down; at the same time, the pressure at -150° , 0° & 150° remains the same value of 1. Thus, one deeper trough presents on the right side and double-peak appears on the left side. And intuitively, the sum of the pressures on the left side is significantly greater than that on the right side.

Magnus effect of different dimensionless spin rate

To explore the effect of different spin rate on the Magnus effect, simulations are performed at $\alpha = 4^\circ$, Mach 1.8, wall temperatures of 300 K and six dimensionless spin rate: $\bar{p} = 0, 0.05, 0.107, 0.151, 0.230 \text{ \& } 0.315$ ($\bar{p} = pd/2u_\infty$) in this part, where p is the spin rate and the u_∞ is freestream velocity. Figure 8 shows the pressure contour of the non-spinning and a spinning model at AOA of 4° . At $\bar{p} = 0$, the pressure is symmetrical. At $\bar{p} = 0.315$, the pressure decreases on one side, increases on the opposite side. Then five planes at x/d equals to 0.5, 1.5, 2.5, 3.5 & 4.5 are cut, and the pressure corresponding to different section is depicted in Figure 9. It can be seen that significant asymmetry of pressure appears at $x/d = 4.5$, which is near the projectile trailing edge, where great focus has been paid around.

The pressure contours with the superimposed cross-flow velocity streamlines at an axial position of $x/d = 4.5$ is presented in Figure 10. The different dimensionless spin rates for these selected cases are $\bar{p} = 0, 0.05, 0.107, 0.151, 0.23 \text{ \& } 0.315$, respectively. For a non-spinning model in Figure 10 (a), the flow field and pressure distribution around the model is symmetric; while for spinning model, the cross-flow velocity field is no longer symmetric (see it in Figure 10 (b) to (f)), so does the pressure field. It can be seen clearly from the figure that the distortion of the boundary layer thickness along the circumferential direction increases with the increasement of the dimensionless spin rate.

In addition, Figure 10 shows that the separation point of the airflow on the left side of the projectile is gradually moving downward as the dimensionless spin rate increases, which can be the main influence mechanism of dimensionless spin rate on the lateral force. The phase angle of the separation point position corresponding to different dimensionless rotation angular velocities is plotted in Figure 11 by numerical fitting. The phase angle (θ) of the separation point is related to the dimensionless spin rate (\bar{p}) by

$$\theta = 71.16\exp(1.334\bar{p}) - 71.07\exp(-13.02\bar{p}) \quad (5)$$

This is the fitting equation with the smallest variance of the data obtained from the current numerical simulation results through different fitting methods. It is suitable for accurately predicting the position of the separation point on the surface of the ANSR corresponding to different dimensionless angular velocities when the Reynolds number is around 8.376×10^5 and the AOA is around 4° . In addition, this equation may also provide a guidance for the change of the separation point with the dimensionless spin rate under other conditions.

The circumferential pressure distribution normalized by the freestream static pressure P_∞ for different spin rates at $x/d = 4.5$ is displayed in Figure 12. When $p = 0$, the model does not spin, the circumferential pressure distribution curve of the projectile is bilaterally symmetric, which approximates a cosine distribution:

$$P_w / P_\infty = 0.972 + 0.02\cos\theta \quad (6)$$

The minimum pressure on both sides appears at θ of $\pm 90^\circ$, and the maximum pressure appear at 0° & $\pm 180^\circ$. As the speed increases, the pressure value decreases within the range of $0^\circ - 90^\circ$, but increases at -90° , which results in an asymmetric distribution. Thus, a lateral force that is directed to the negative z-axis, is generated on the projectile and the magnitude of this force increases as the rotational speed increases. Therefore, it can be considered that the magnitude of the Magnus force is positively correlated with the dimensionless spin rate. In addition, when the dimensionless spin rate exceeds a certain value, more than one trough appears on the left curve. This implies a complicated flow phenomenon on the left side.

To explore the quantitative relationship between the Magnus force and the dimensionless spin rate, the Magnus force at different speeds is plotted in Figure 13. It can be seen that the numerical simulation results agree well with the experimental values, and every experimental

result and simulation result data point almost falls on the fitted straight line. The Magnus force coefficient C_y values, corresponding to different spin rate at the 4° AOA, are distributed around the straight line, with a slope -0.126:

$$C_y = -0.126\bar{p} \quad (7)$$

Therefore, it can be approximated that the magnitude of the Magnus force of ANSR is proportional to the dimensionless spin rate when the Reynolds number is around 8.376×10^5 and the AOA is around 4° .

Magnus effect of different wall temperature

In view of the fact that the work of the predecessors hardly consider the influence of temperature on the Magnus effect, this part of the work studies the different wall temperature effects on the Magnus effect. This is very significant for studying the aerodynamic stability of high-speed rotating rocket with significant external aerodynamic and internal engine heat problems, especially close to the trailing edge.

For Figure 14 and Figure 15 a, b, c and d, the wall temperature equals to 300 K, 600 K, 900 K & 1200 K, respectively. It can be seen from the pressure contour that when the wall temperature increases, the asymmetry of the pressure on the left and right sides of the wall decreases slightly. From the temperature contour it can be seen that the temperature around the wall, especially at the position between -90° - -45° and 0° - 120° , is significantly increased.

And it can be seen from the trend of the curve in Figure 16 that the pressure is significantly increased in the region where the temperature is significantly increased, and the sum of the increase in the right pressure is greater than that on the left side. Thereby the Magnus effect is reduced with the increasing temperature.

The temperature fields for different wall temperatures are shown in Figure 17. The increase in wall temperature leads to a significant change in the state of the temperature boundary layer, and the motion of walls inject momentum to the flow, which extensively changes the flow and heat transfer patterns and the aerodynamic forces [23], which affects the Magnus effect.

It can be seen from Figure 18 (a) that the Magnus force coefficient C_y values corresponding to different wall temperatures at 1.8 Mach, spin rate $\bar{p} = 0.315$ and $\alpha = 8^\circ$ are distributed around the straight line:

$$C_y = 5.528 \times 10^{-6} T_w - 0.1096 \quad (8)$$

Although the coefficient of the first term in equation (8) is very small, the Magnus effect decreases obviously with the increasing wall temperature. Therefore, in sensitive cases, the influence of the wall temperature on the Magnus effect cannot be ignored. As the temperature increases, it can also be seen from Figures 18 (b), (c) that the lift coefficient increases and the drag coefficient drops significantly, which indicates a relatively high surface temperature has a positive effect on aerodynamic performance and flight stability control.

The largest pressure variation is between $\theta = -50^\circ$ to -70° . A typical wall normal temperature distribution at $\theta = -70^\circ$ is plotted in Figure 19, where the wall temperature has a strong impact on the thermal boundary layer, thus the Magnus effect.

Conclusions

In this paper, three different eddy-viscous models are verified by a fully developed turbulent channel flow case at $Re_\tau = 590$ firstly. The results illustrate that k- ϵ Yang-Shih model [18] provides the best solutions than others for RANS wall-bounded turbulence modeling, in terms of the logarithmic velocity distribution, turbulent kinetic energy, Reynolds shear stress and

turbulent viscosity. These ensure an accurate prediction of the near-wall flow characteristics of the spinning rocket, and the subsequent results also confirm it.

Three sets of parametric studies have been carried out on the three-dimensional ANSR model. The current simulation results clearly approximate the experimental values better than the numerical solution in the existing references [5]. The magnitude of the Magnus force is approximately proportional to the dimensionless spin rate, $C_y = -0.12 \bar{p}$, at the AOA of 4° . In addition, the simulations provide a profound insight into the flow pattern and reveal that the separation point of the airflow on the left side of the projectile moves gradually downward as the dimensionless spin rate increases, however almost unchanged with the angles of attack. The distortion of the boundary layer thickness is the main factor affecting the magnitude of the Magnus force at different angles of attack. Furthermore, the current study suggests that relatively higher surface temperature has a positive effect on reducing the Magnus and drag forces, but on slightly increasing the lift force.

Nomenclature

<i>ANSR</i>	Army-Navy Spinner Rocket
<i>AOA</i>	angle of attack
<i>BSL</i>	Baseline
<i>c</i>	speed of sound, m/s
C_d	drag coefficient, $2F_d/u_\infty^2 S$
C_l	lift coefficient, $2F_l/u_\infty^2 S$
C_y	Magnus force coefficient, $2F_y/u_\infty^2 S$
C_{yp}	Magnus force coefficient, C_y/\bar{p}

C_{ypR}	Original Magnus force coefficient in references
$C_{1\epsilon}$	constant in Eq. (3)
$C_{2\epsilon}$	constant in Eq. (3)
c_μ	constant in Eq. (2)
CFD	computational fluid dynamics
d	diameter, mm
d_w	distance from the wall, mm
DNS	direct numerical simulation
E	secondary source term
e	total energy per unit volume, J/m ³
EWT	Enhanced wall treatment
F_d	drag force, N
F_l	lift force, N
F_y	Magnus force, N
h	half the width of the channel, m
k	turbulent kinetic energy, m ² /s ²
k^+	dimensionless turbulent kinetic energy, k/u_τ^2
l	model length, m
Ma	Mach number, u_∞/c
N_b	node number in the O-shaped boundary layer region
N_c	node number in the circumferential direction
N_{in}	node number between the inlet and the model nose
N_l	node number in the streamwise direction

N_{out}	node number between the end of the model and the outlet
N_{1r}	node number in radial direction of the C-shaped region
N_{2r}	node number radial direction of outside the C-shaped region
P	static pressure, Pa
P_w	wall pressure, Pa
P_∞	freestream static pressure, Pa
p	spin rate, rad/s
\bar{p}	dimensionless spin rate, $pd/2u_\infty$
q	heat flux, W/m^2
R	specific gas constant, $J \cdot kg/K$
<i>RNG</i>	Re-normalization Group
Re	Reynolds number, $\rho u_\infty d/\mu$
Re_τ	friction Reynolds number, $\rho u_\tau d/\mu$
<i>Ref</i>	references
<i>RANS</i>	Reynolds-averaged Navier-Stokes
S	reference area, m^2
<i>SST</i>	Shear-Stress Transport
T	temperature, K
T_t	time scale
T_w	wall temperature, K
t	time, s
u	velocity in x direction, m/s
u_i	Favre averaged velocities, m/s

u_j	Favre averaged velocities, m/s
u_τ	wall friction velocity, $[(du/dy)/\rho]^{1/2}$, m/s
u_∞	freestream velocity, m/s
u^+	dimensionless velocity, u/u_τ
u'	fluctuating velocity in x direction, m/s
v'	fluctuating velocity in y direction, m/s
X	X-coordinate, denote the streamwise direction
x	x-coordinate value, m
x_i	length vector, m
x_j	length vector, m
Y	Y-coordinate, denote the transverse direction
y	y-coordinate value, m
y^+	dimensionless wall distance, $\rho u_\tau y/\mu$
Z	Z-coordinate, denote the spanwise direction

Greek symbols

α	angle of attack, °
δ_{ij}	Kronecker delta
ε	dissipation rate, defined by Eq. (3)
μ	dynamic viscosity, N/m ² s
μ_T	eddy viscosity, N/m ² s
θ	phase angle along the body, °
ρ	density, kg/m ³

σ_k	constant in Eq. (3)
σ_ε	constant in Eq. (3)
ω	specific rate of dissipation

Subscripts

c	circumferential direction
b	boundary layer
in	<i>inlet</i>
i, j	spacial index
k	turbulent kinetic energy
l	lift
out	outlet
Ref	references
$1r$	radial direction of C-shaped region
$2r$	radial direction out of C-shaped region
w	wall
y	lateral force
yp	Ratio of lateral force to rotation speed
ypR	Original Ratio of lateral force to rotation speed in references
∞	freestream
ε	dissipation rate
μ	dynamic viscosity
τ	viscous stress

Acknowledgements

The grant support from the National Science Foundation of China (No. 11532002) is greatly acknowledged.

References

- [1] C. H. Murphy and L. E. Schmidt, *The effect of length on the aerodynamic characteristics of bodies of revolution in supersonic flight*, U.S. Army Ballistics Research Laboratory, BRL-R-876, Aberdeen Proving Ground, MD, August, 1953.
- [2] L. E. Schmidt and C. H. Murphy, *The aerodynamic properties of the 7-caliber army-navy spinner rocket in transonic flight*, U.S. Army Ballistics Research Laboratory, BRL-MR-775, Aberdeen Proving Ground, MD, March, 1954.
- [3] O. Donneaud, C. Chemiere, R. Cayzac, and P. Champigny, “Recent developments on aeroballistics of yawing and spinning projectiles. Part II - Free Flight Tests,” *20th International Symposium on Ballistics, Orlando, FL*, pp. 23-27, 2002.
- [4] W. Luchuk and W. Sparks, *Wind-Tunnel Magnus characteristics of the 7-Caliber Army-Navy Spinner Rocket*, U.S. Naval Ordnance Laboratory, White Oak, MD, NAVORD Technical Report, No.3813, 1954.
- [5] D. Klatt and R. Hruschka, “Numerical and experimental investigation of the Magnus effect in supersonic flows,” *30th AIAA Applied Aerodynamics Conference*, New Orleans, Louisiana, 25 - 28 June 2012.

- [6] A. S. Platou, "Magnus characteristics of finned and nonfinned projectiles," *AIAA Journal*, vol.3, no. 1, pp. 83-90, 1965. DOI:10.2514/3.2791.
- [7] J. DeSpirito, S. I. Sidra and P. Weinacht, "Navier-Stokes predictions of dynamic stability derivatives: evaluation of steady-state methods," *Journal of Spacecraft and Rockets*, vol.46, no. 6, pp. 1142-1154, 2009. DOI: 10.2514/1.38666.
- [8] M. Pechier, P. Guillen and R. Cayzac, "A combined theoretical-experimental investigation of Magnus effects," *16th AIAA Applied Aerodynamics Conference*, Albuquerque, NM, 15 - 18 June 1998.
- [9] S. I. Sifton, "Navier-stokes computations for a spinning projectile from subsonic to supersonic speeds," *Journal of Spacecraft and Rockets*, vol.42, no.2, pp. 223-231, 2005. DOI: 10.2514/1.4175.
- [10] J. DeSpirito, and H. Karen, "CFD computation of Magnus moment and roll-damping moment of a spinning projectile," *AIAA atmospheric flight mechanics conference and exhibit*, Providence, Rhode island, 16 - 19 August 2004.
- [11] J. DeSpirito, and P. Plostins, "CFD prediction of M910 projectile aerodynamics: unsteady wake effect on Magnus moment," *AIAA atmospheric flight mechanics conference and exhibit*, Hilton Head, South Carolina, 20 - 23 August 2007.
- [12] J. DeSpirito, "CFD prediction of Magnus effect in subsonic to supersonic flight," *46th AIAA Aerospace Sciences Meeting and Exhibit*, Reno, Nevada, 7 - 10 January 2008.
- [13] K. Y. Chien, "Predictions of channel and boundary layer flows with a low-Reynolds number turbulence model," *AIAA Journal*, vol.20, no.1, pp. 33-38, 1982. DOI: 10.2514/3.51043.

- [14] H. A. Daud, Q. LI, O. A. Beg, and S. A. AbdulGhani, "Numerical investigations of wall-bounded turbulence," *Journal of Mechanical Engineering Science*, vol.225, no.5, pp. 1163-1174, 2011. DOI: 10.1177/09544062jmes2524.
- [15] S. M. Hashemian, M. Rahnama, and M. Farhadi, "Large eddy simulation of turbulent heat transfer in a channel with a square cylinder," *Heat Transfer Engineering*, vol. 33, no.12, pp. 1052-1062, 2012. DOI: 10.1080/01457632.2012.659630.
- [16] R. D. Moser, J. Kim and N. N. Mansour, "Direct numerical simulation of turbulent channel flow up to $Re = 590$," *Physics of Fluids*, vol.11, no. 4, pp. 943-945, 1999. DOI: 10.1063/1.869966.
- [17] B. E. Launder, and D. B. Spalding, "The numerical computation of turbulent flows," *Computer Methods in Applied Mechanics and Engineering*, vol.3, no.2, pp. 269-289, 1974. DOI: 10.1016/b978-0-08-030937-8.50016-7.
- [18] Z. Yang, and T. H. Shih, "New time scale based k-epsilon model for near-wall turbulence," *AIAA Journal*, vol. 31, no. 7, pp. 1191-1198, 1993. DOI: 10.2514/3.11752.
- [19] W. Rodi, and N. N. Mansour, "Low Reynolds number k- ϵ modelling with the aid of direct simulation data," *Journal of Fluid Mechanics*, vol.250, pp. 509-529, May 1993. DOI:10.1017/s0022112093001545.
- [20] D. C. Wilcox, *Turbulence modeling for CFD*, vol. 2, La Canada, CA: DCW industries, 1998.
- [21] P. L. Roe, "Approximate Riemann solvers, parameter vectors, and difference schemes," *Journal of computational physics*, vol. 43, no. 2, pp. 357-372, 1981. DOI: 10.1016/0021-9991(81)90128-5.
- [22] J. D. Iversen, "Correlation of Magnus force data for slender spinning cylinders," *Journal of Spacecraft and Rockets*, vol. 10, no.4, pp. 268-272, 1973. DOI: 10.2514/3.61877.

[23] J. Ghazanfarian, "Introducing the Sliding-Wall Concept for Heat Transfer Augmentation: The Case of Flow over Square Cylinder at Incidence," *Heat Transfer Engineering*, vol. 41, no.8, pp. 751-764, 2020. DOI: 10.1080/01457632.2018.1564209.

Table 1. Overview of the computational mesh characteristics.

Mesh	Mesh1	Mesh2	Mesh3
Elements	6.55×10^6	1.52×10^7	2.53×10^7
$N_{in}/$ stretching ratios	51/1.2	65/1.15	65/1.15
N_l	195	220	341
$N_c/$ stretching ratios	200/1	280/1	320/1
$N_b/$ stretching ratios	64/1.13	80/1.09	91/1.09
$N_{1r}/$ stretching ratios	21/1.1	25/1.08	41/1.08
$N_{2r}/$ stretching ratios	41/1.17	65/1.1	65/1.1
$N_{out}/$ stretching ratios	51/1.22	81/1.12	221/1.12
First Boundary layer edge	$2.5 \times 10^{-5}d$	$2.5 \times 10^{-5}d$	$2 \times 10^{-5}d$
y^+	0.4	0.4	0.32

Table 2 Parametric study of magus effects.

Parameters	Test cases conditions
Spin rate	$\alpha = 4^\circ$, 1.8Ma, $T_w = 300$ K, $\bar{p} = 0, 0.05, 0.107, 0.151, 0.230$ & 0.315 .
AOA	1.8Ma, $\bar{p} = 0.315$, $T_w = 300$ K, $\alpha = 0^\circ, 2^\circ, 4^\circ, 6^\circ, 8^\circ$ & 10° .
Wall temperature	1.8Ma, $\bar{p} = 0.315$, $\alpha = 8^\circ$, $T_w = 300$ K, 600 K, 900 K & 1200 K.

List of Figure Captions

Figure 1. Fully developed turbulent channel flow validation at $Re_\tau = 590$.

Figure 2. Geometry model: ANSR model with length $7d$ [2, 12].

Figure 3. Schematic of the structured mesh (a) overall; (b) the symmetry plane; (c) near the rocket.

Figure 4. Lateral force corresponding to different meshes, $\alpha = 8^\circ$

Figure 5. Dimensionless lateral force vs. AOA.

Figure 6. The AOA effect vs. boundary layer distortion (coloured with pressure and streamline on the plane of $x/d = 4.5$ ((a) $\alpha = 0^\circ$; (b) $\alpha = 2^\circ$; (c) $\alpha = 4^\circ$; (d) $\alpha = 6^\circ$; (e) $\alpha = 8^\circ$; (f) $\alpha = 10^\circ$, respectively, at $Ma = 1.8$ and $\bar{p} = 0.315$).

Figure 7. The effect of AOA on wall pressure at $x/d = 4.5$.

Figure 8. Surface pressure contours of the non-spinning ($\bar{p} = 0$) and spinning ($\bar{p} = 0.315$) rockets at $\alpha = 4^\circ$.

Figure 9. Circumferential pressure distribution at the different sections.

Figure 10. The $Ma = 1.8$, $\alpha = 4$ pressure contours and streamline on the plane of $x/d = 4.5$ (a) $\bar{p} = 0$; (b) $\bar{p} = 0.05$; (c) $\bar{p} = 0.107$; (d) $\bar{p} = 0.151$; (e) $\bar{p} = 0.230$ and (f) $\bar{p} = 0.315$.

Figure 11. Location of the separation point.

Figure 12. Wall pressure profile at $x/d = 4.5$ for different spin rate, \bar{p} .

Figure 13. Magnus force coefficient C_y against dimensionless spin rate \bar{p} at $Ma = 1.8$ and $\alpha = 4^\circ$.

Figure 14. $Ma = 1.8$, $\bar{p} = 0.315$, $\alpha = 8$, pressure contours and streamlines at $x/d = 4.5$: (a) $T_w = 300$ K; (b) $T_w = 600$ K; (c) $T_w = 900$ K & (d) $T_w = 1200$ K, respectively.

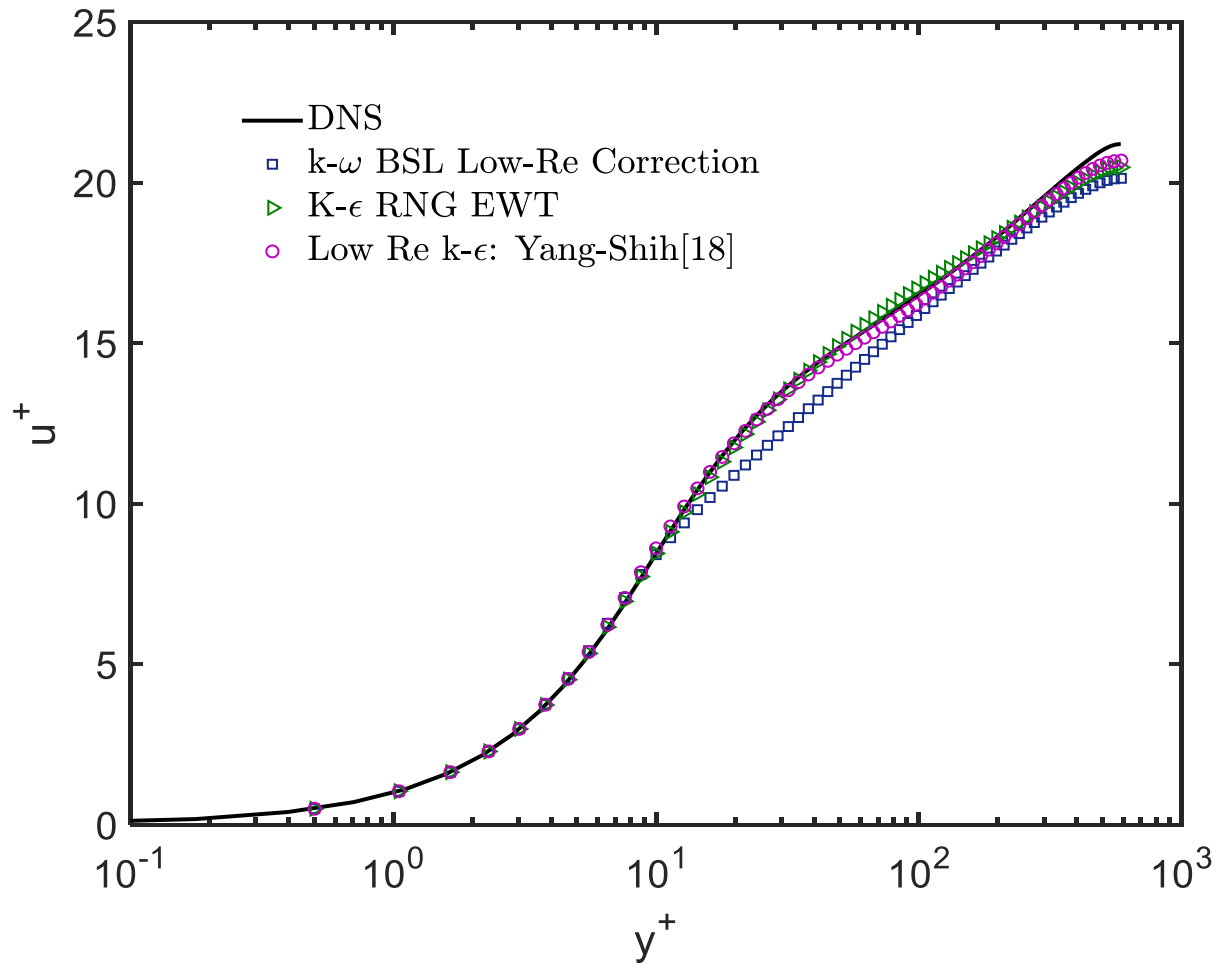
Figure 15. $Ma = 1.8$, $\bar{p} = 0.315$, $\alpha = 8$, temperature contours and streamlines at $x/d = 4.5$ (a) $T_w = 300$ K; (b) $T_w = 600$ K; (c) $T_w = 900$ K & (d) $T_w = 1200$ K, respectively.

Figure 16. The effect of wall temperature on the wall pressure at $x/d = 4.5$.

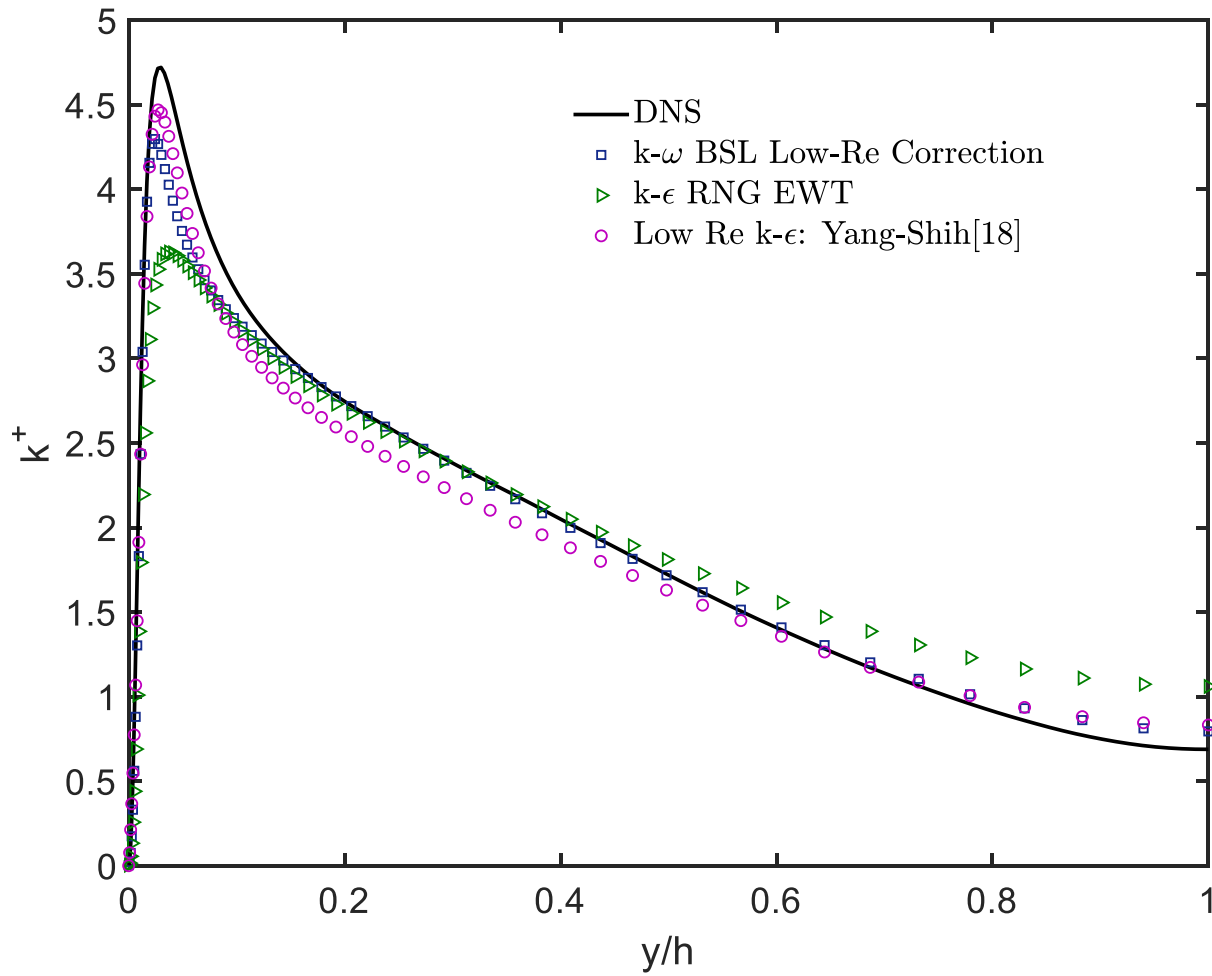
Figure 17. Temperature effect at $Ma = 1.8$, $\bar{p} = 0.315$ and $\alpha = 8$.

Figure 18. $Ma = 1.8$ and $\bar{p} = 0.315$: (a) C_{yp} ; (b) C_i ; (c) C_d against different wall temperature.

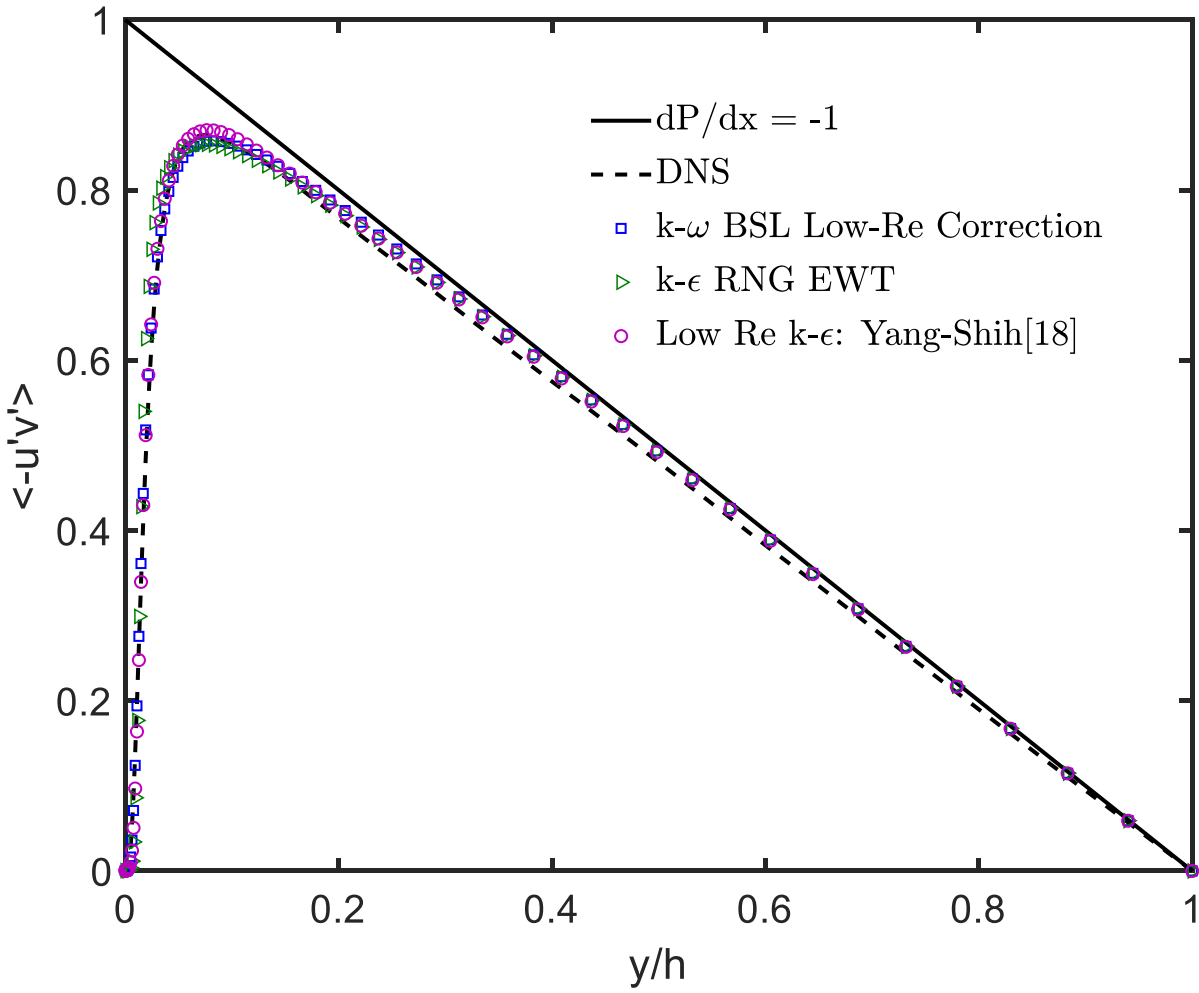
Figure 19. Wall temperature effect on the thermal boundary layer profile at $\bar{p} = 0.315$ ($\theta = -70^\circ$).



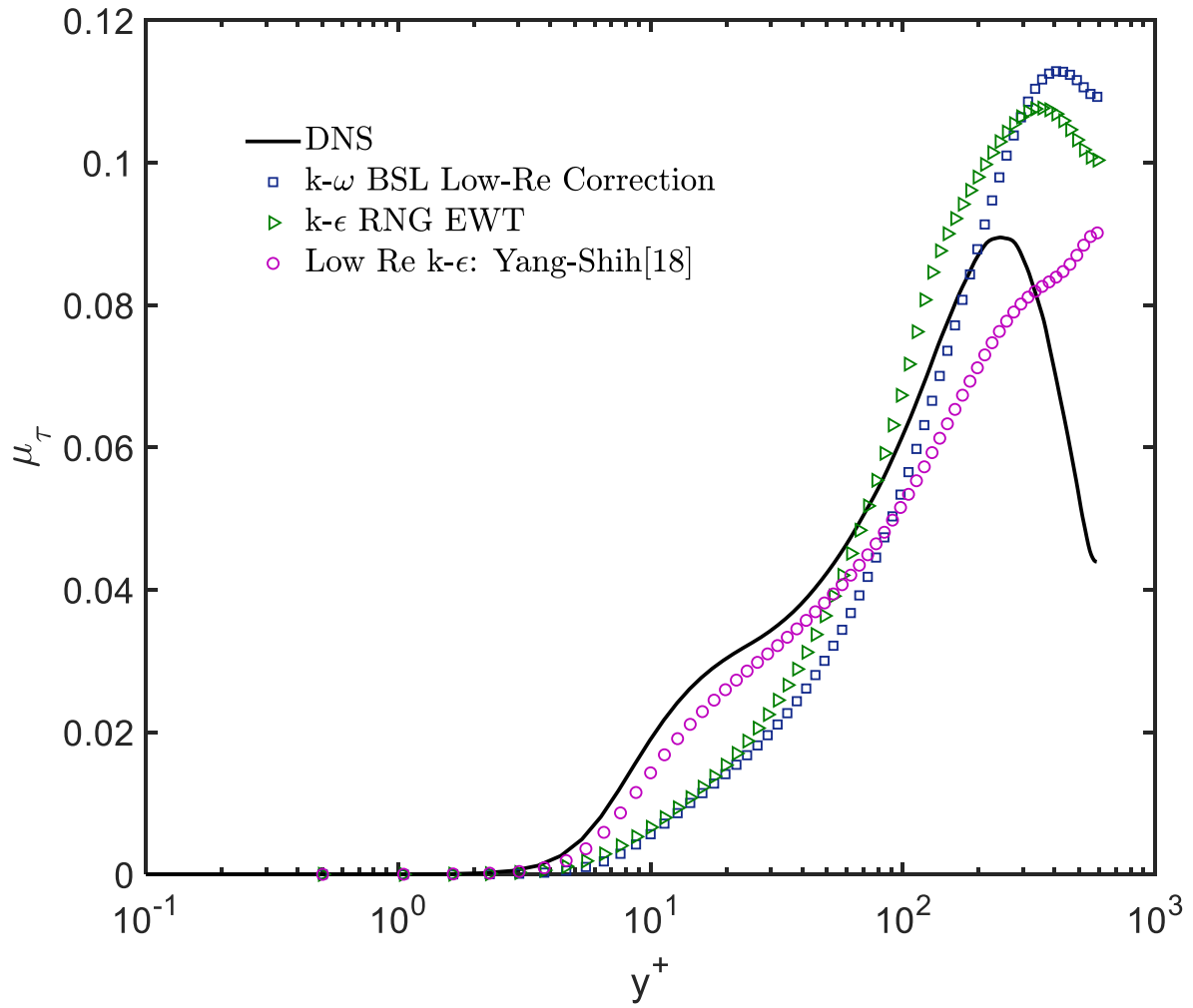
(a) Turbulent mean velocity.



(b) Turbulent kinetic energy.



(c) Reynolds shear stress.



(d) Turbulent viscosity.

Figure 1. Fully developed turbulent channel flow validation at $Re_\tau = 590$.

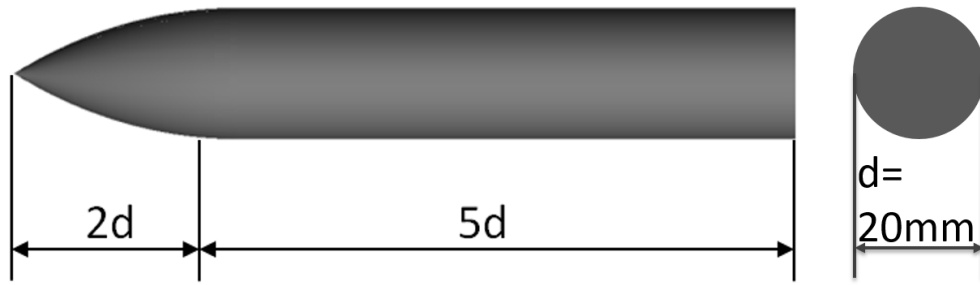
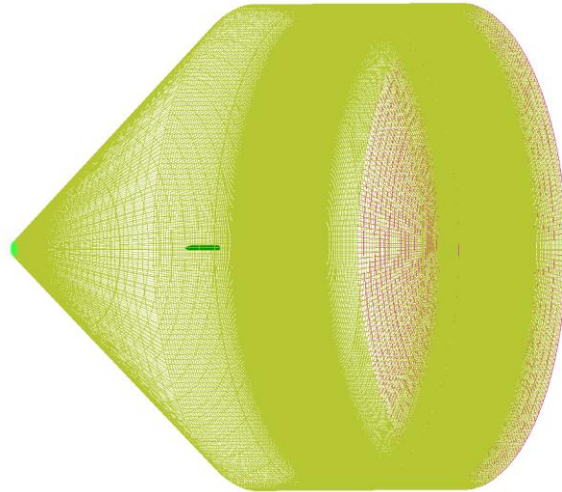
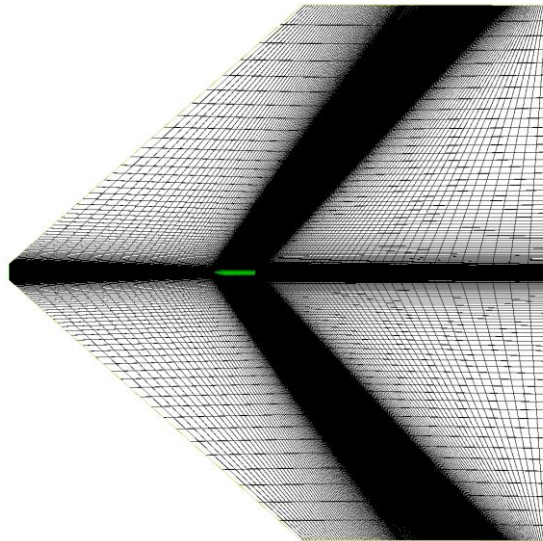


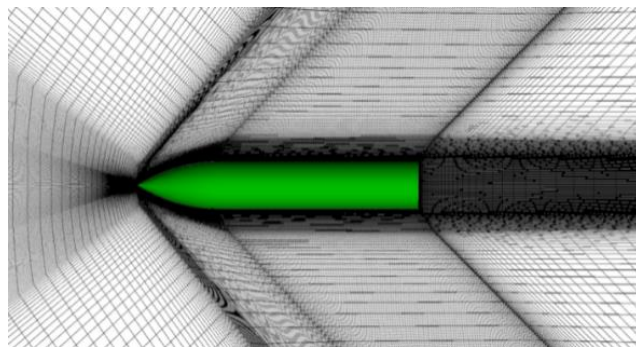
Figure 2. Geometry model: ANSR model with length $7d$ [2, 12].



(a)



(b)



(c)

Figure 3. Schematic of the structured mesh (a) overall; (b) the symmetry plane; (c) near the rocket.

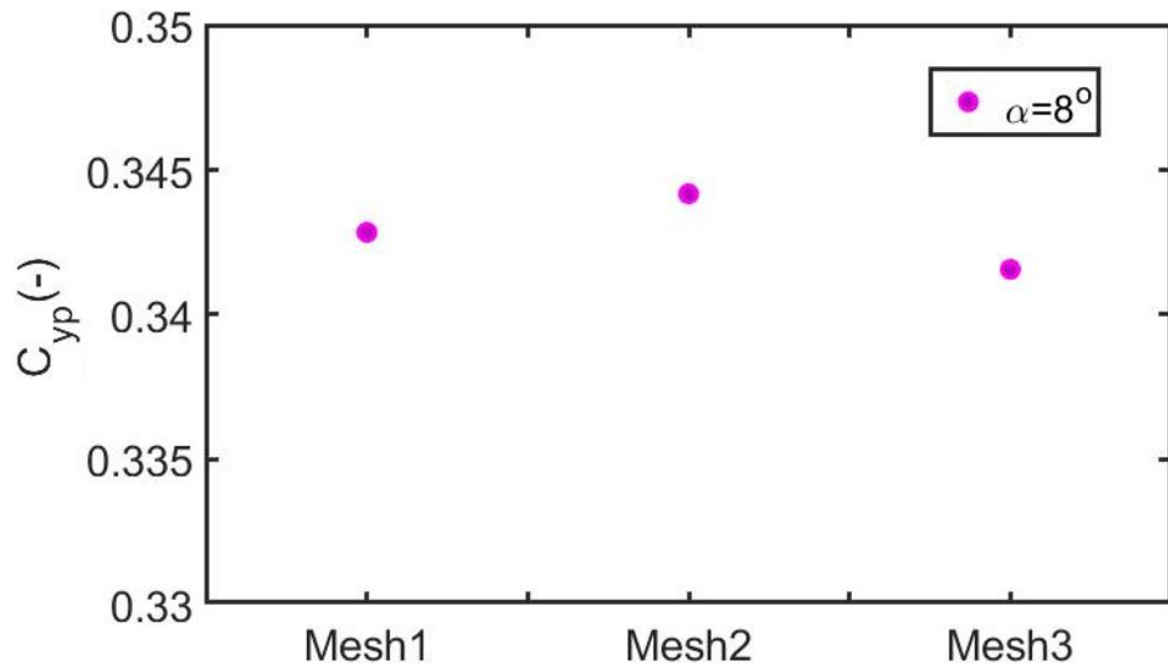


Figure 4. Lateral force corresponding to different meshes, $\alpha = 8^\circ$

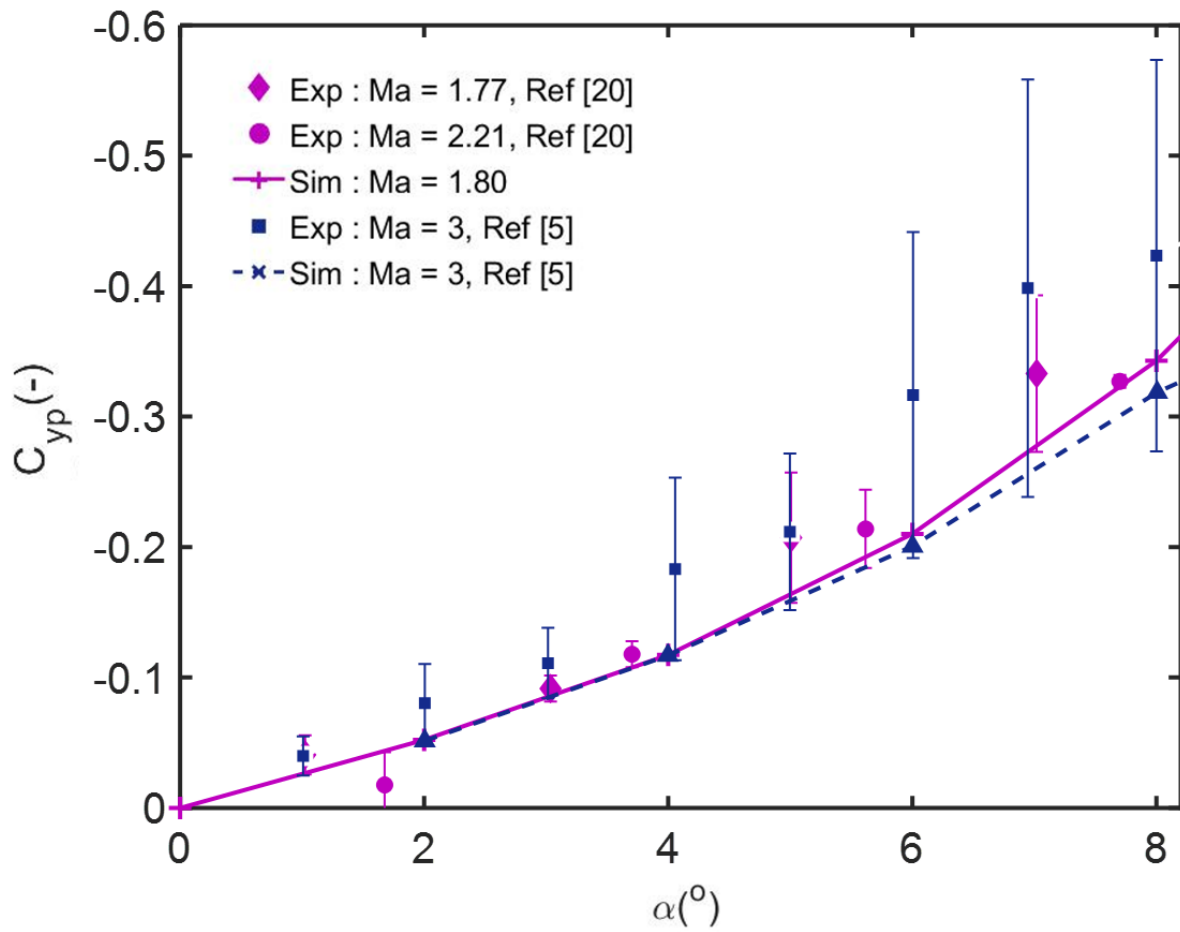


Figure 5. Dimensionless lateral force vs. AOA.

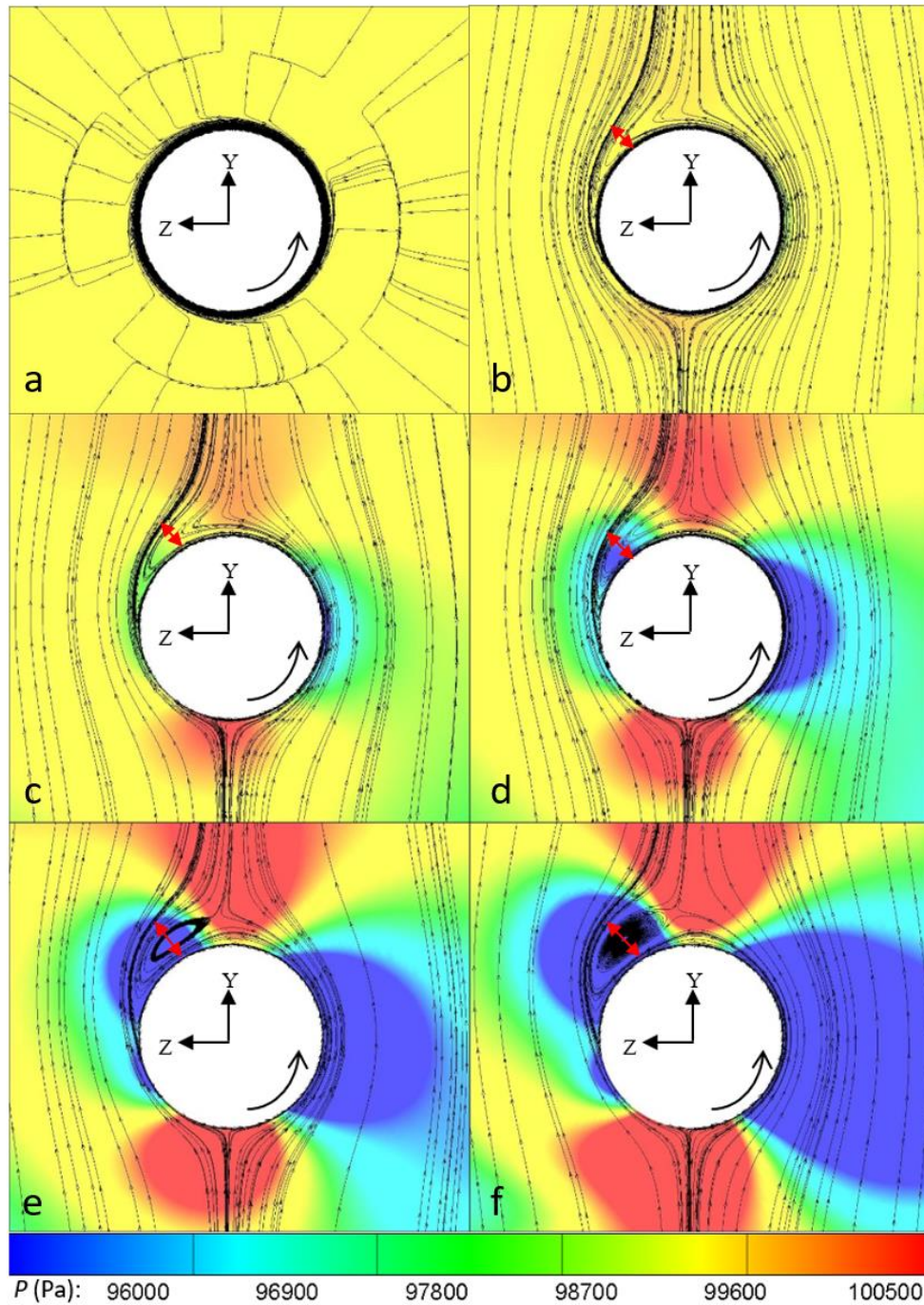


Figure 6. The AOA effect vs. boundary layer distortion (coloured with pressure and streamline on the plane of $x/d = 4.5$ ((a) $\alpha = 0^\circ$; (b) $\alpha = 2^\circ$; (c) $\alpha = 4^\circ$; (d) $\alpha = 6^\circ$; (e) $\alpha = 8^\circ$; (f) $\alpha = 10^\circ$, respectively, at $Ma = 1.8$ and $\bar{p} = 0.315$).

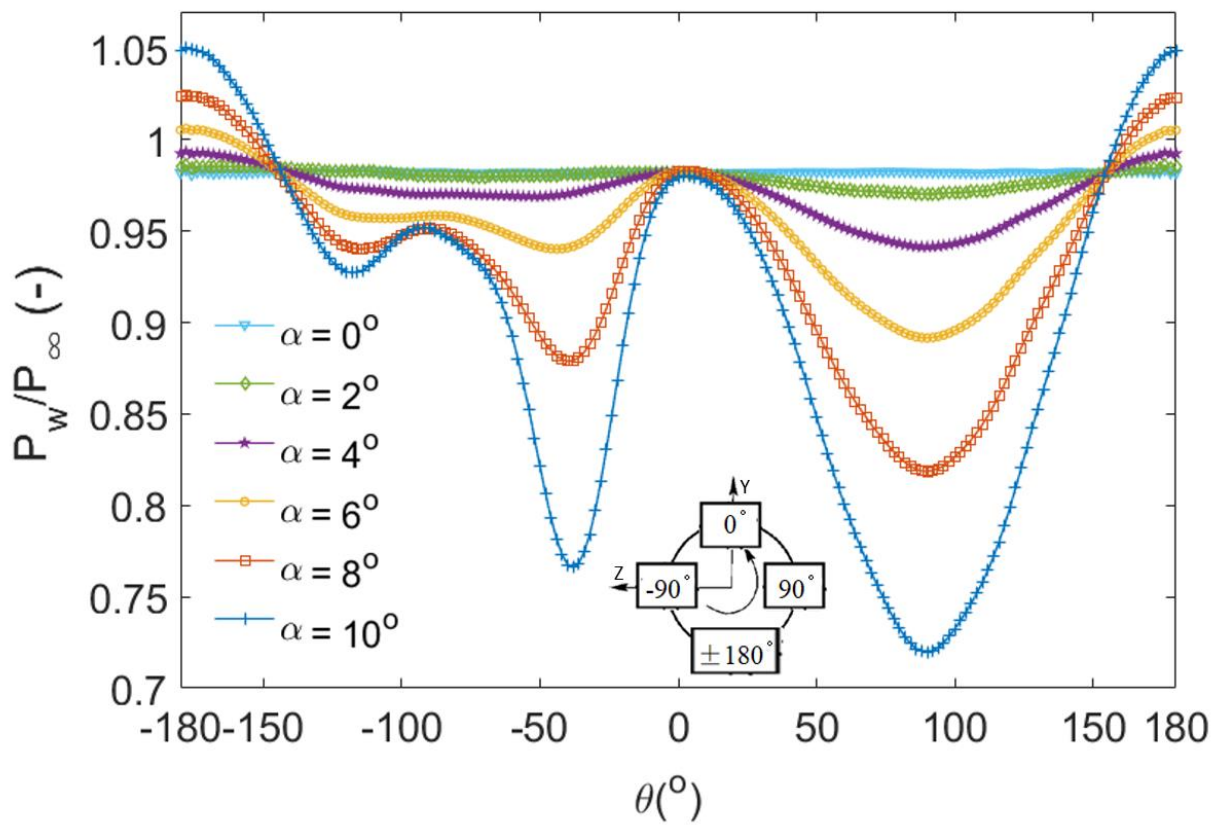


Figure 7. The effect of AOA on wall pressure at $x/d = 4.5$.

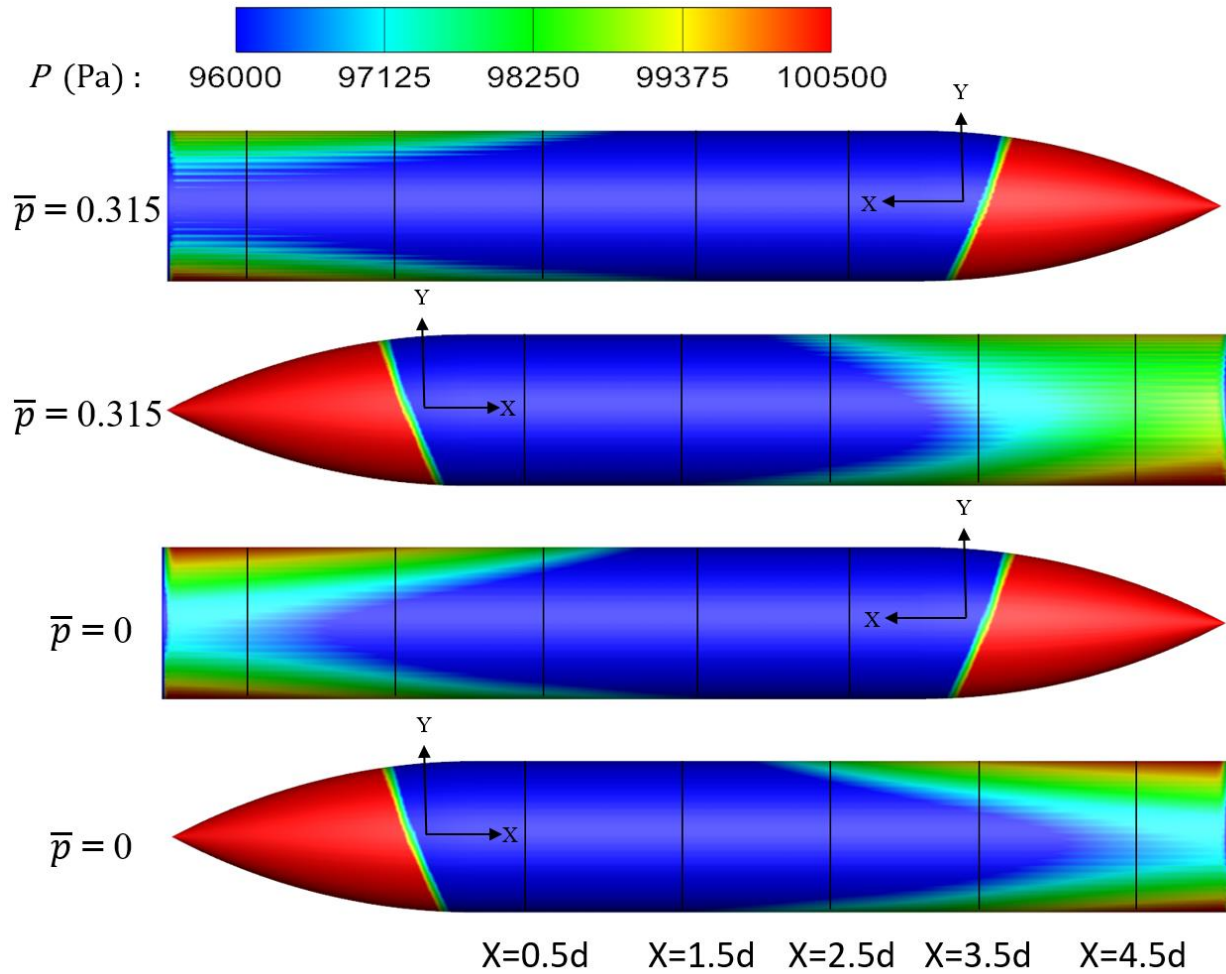


Figure 8. Surface pressure contours of the non-spinning ($\bar{p} = 0$) and spinning ($\bar{p} = 0.315$) rockets at $\alpha = 4^\circ$.

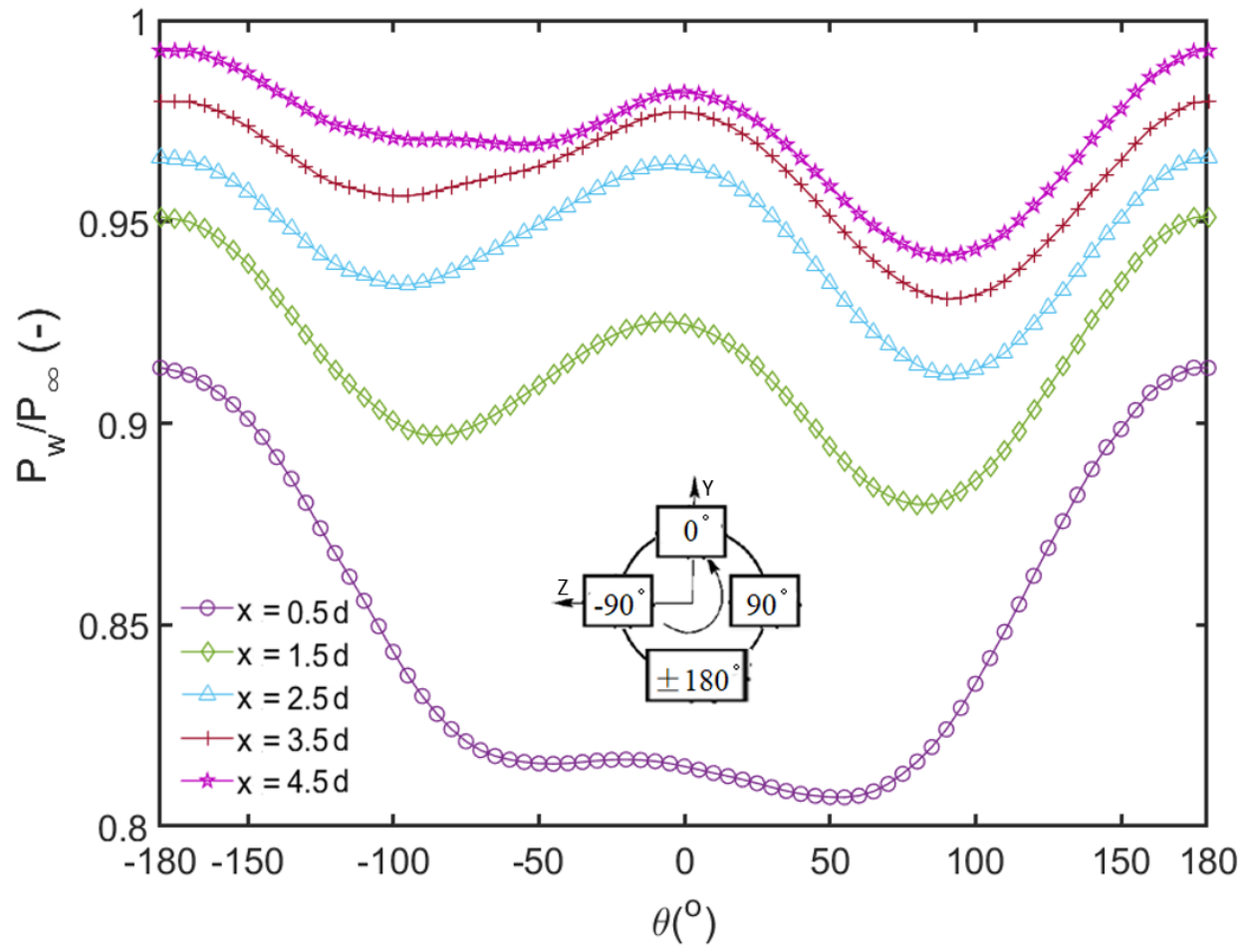


Figure 9. Circumferential pressure distribution at the different sections.

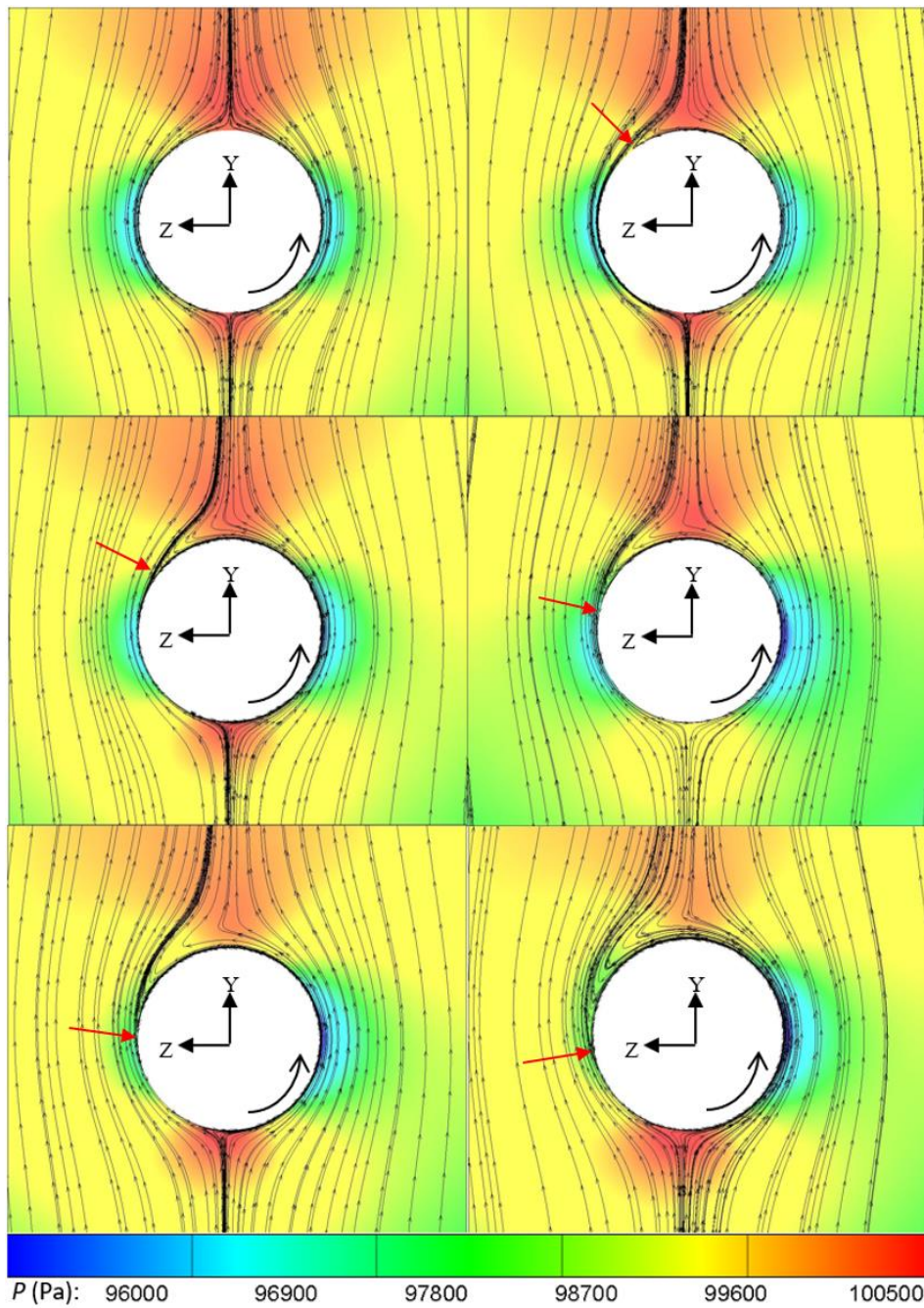


Figure 10. The $Ma=1.8$, $\alpha=4$ pressure contours and streamline on the plane of $x/d=4.5$

(a) $\bar{p} = 0$; (b) $\bar{p} = 0.05$; (c) $\bar{p} = 0.107$; (d) $\bar{p} = 0.151$; (e) $\bar{p} = 0.230$ and (f) $\bar{p} = 0.315$.

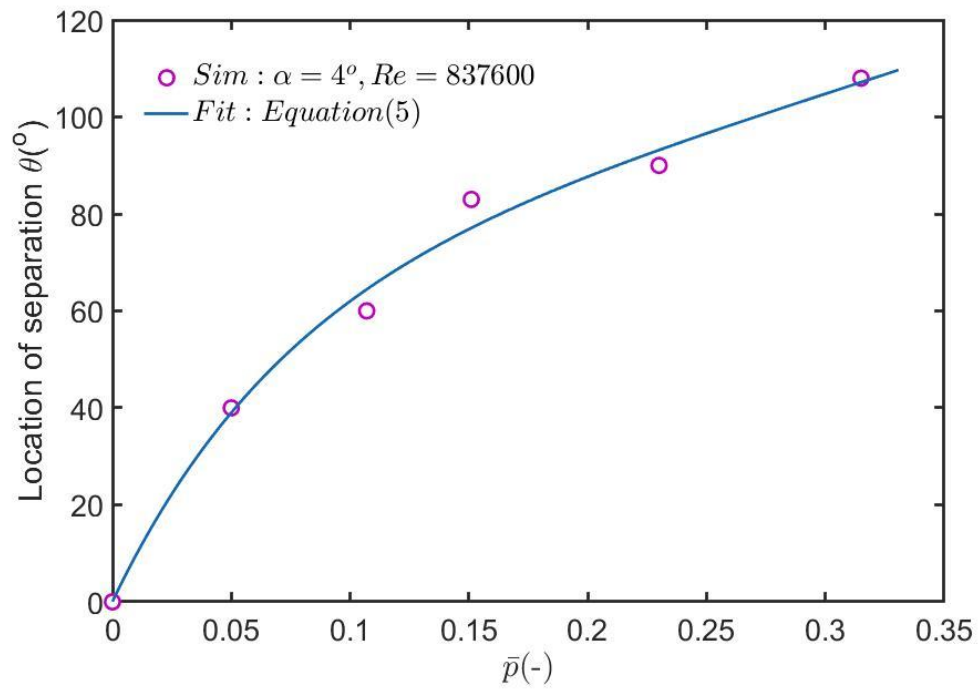


Figure 11. Location of the separation point.

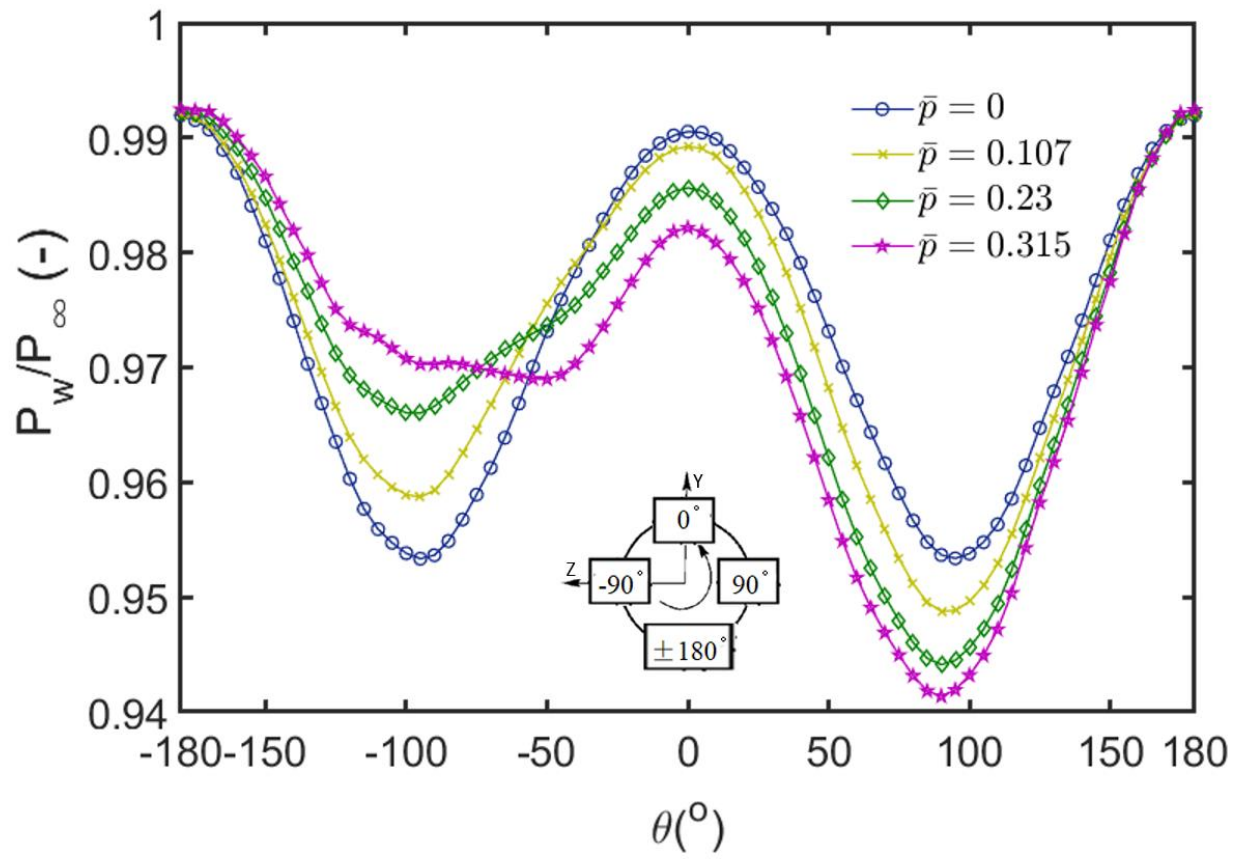


Figure 12. Wall pressure profile at $x/d = 4.5$ for different spin rate, \bar{p} .

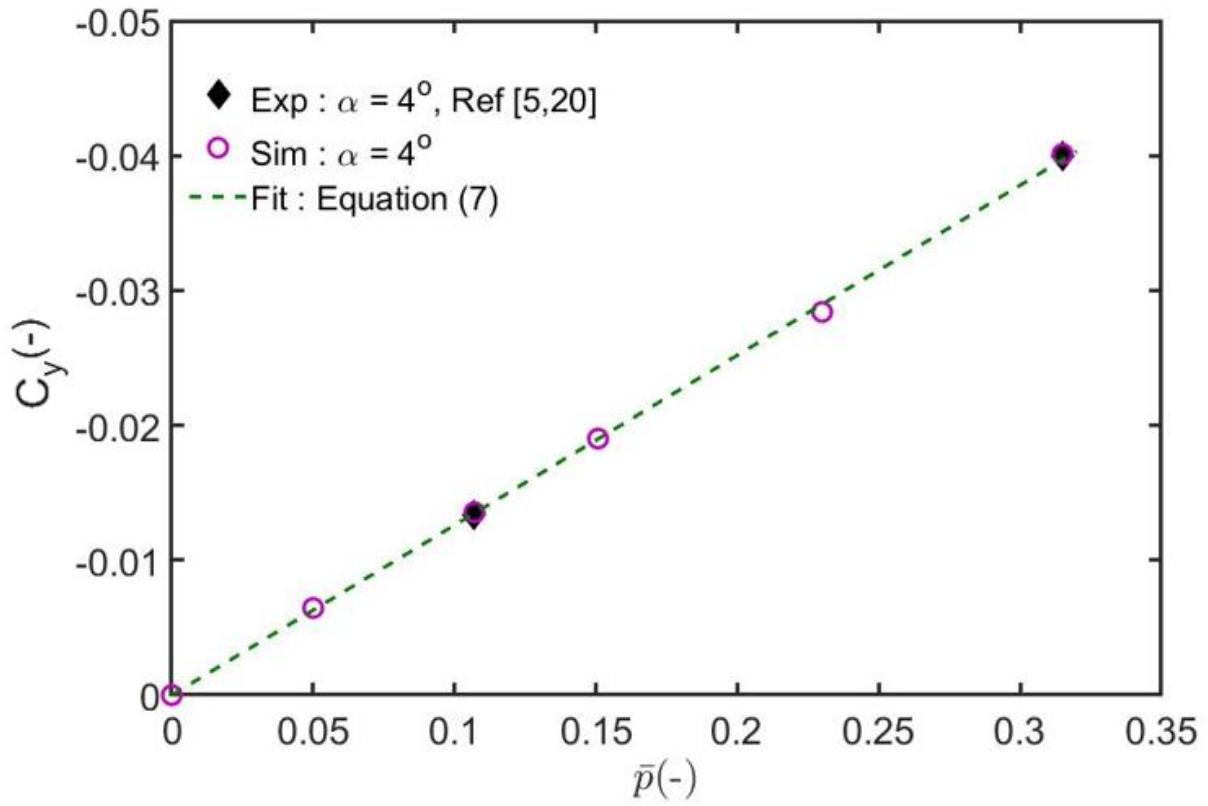


Figure 13. Magnus force coefficient C_y against dimensionless spin rate \bar{p} at $Ma = 1.8$ and $\alpha = 4^\circ$.

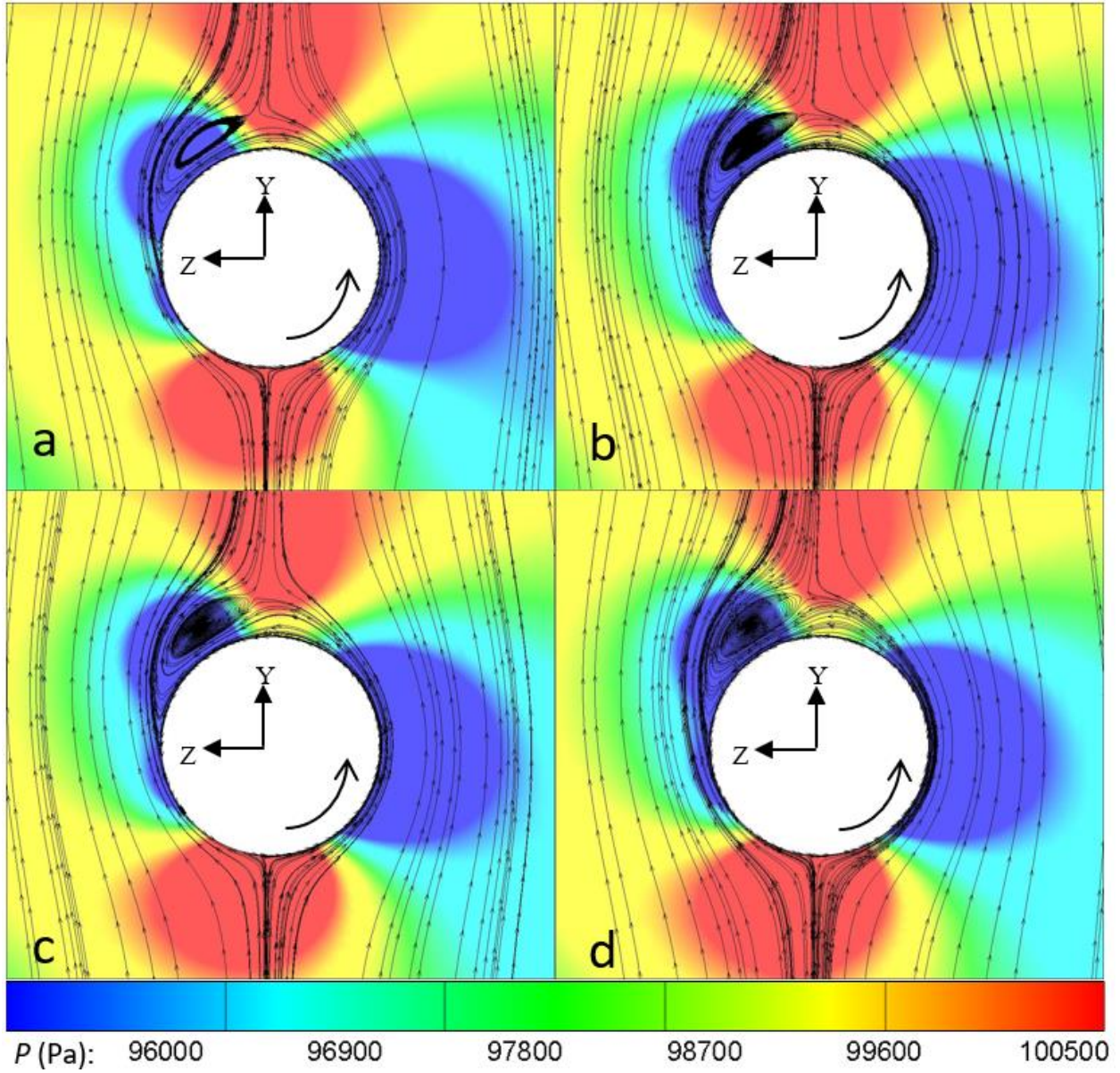


Figure 14. $Ma = 1.8$, $\bar{p} = 0.315$, $\alpha = 8$, pressure contours and streamlines at $x/d = 4.5$: (a) $T_w = 300$ K; (b) $T_w = 600$ K; (c) $T_w = 900$ K & (d) $T_w = 1200$ K, respectively.

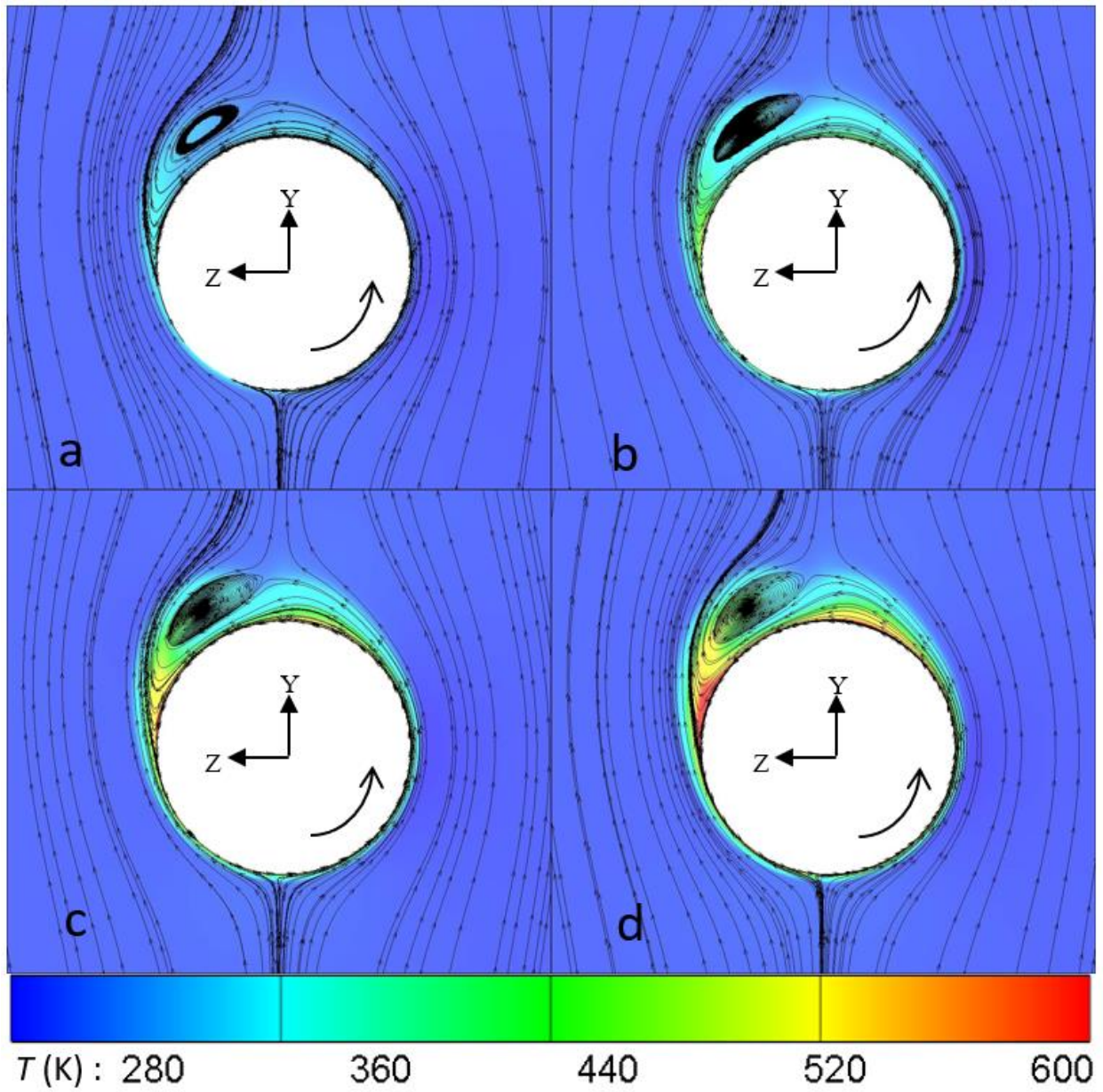


Figure 15. $Ma = 1.8$, $\bar{p} = 0.315$, $\alpha = 8$, temperature contours and streamlines at $x/d = 4.5$: (a) $T_w = 300$ K; (b) $T_w = 600$ K; (c) $T_w = 900$ K & (d) $T_w = 1200$ K, respectively.

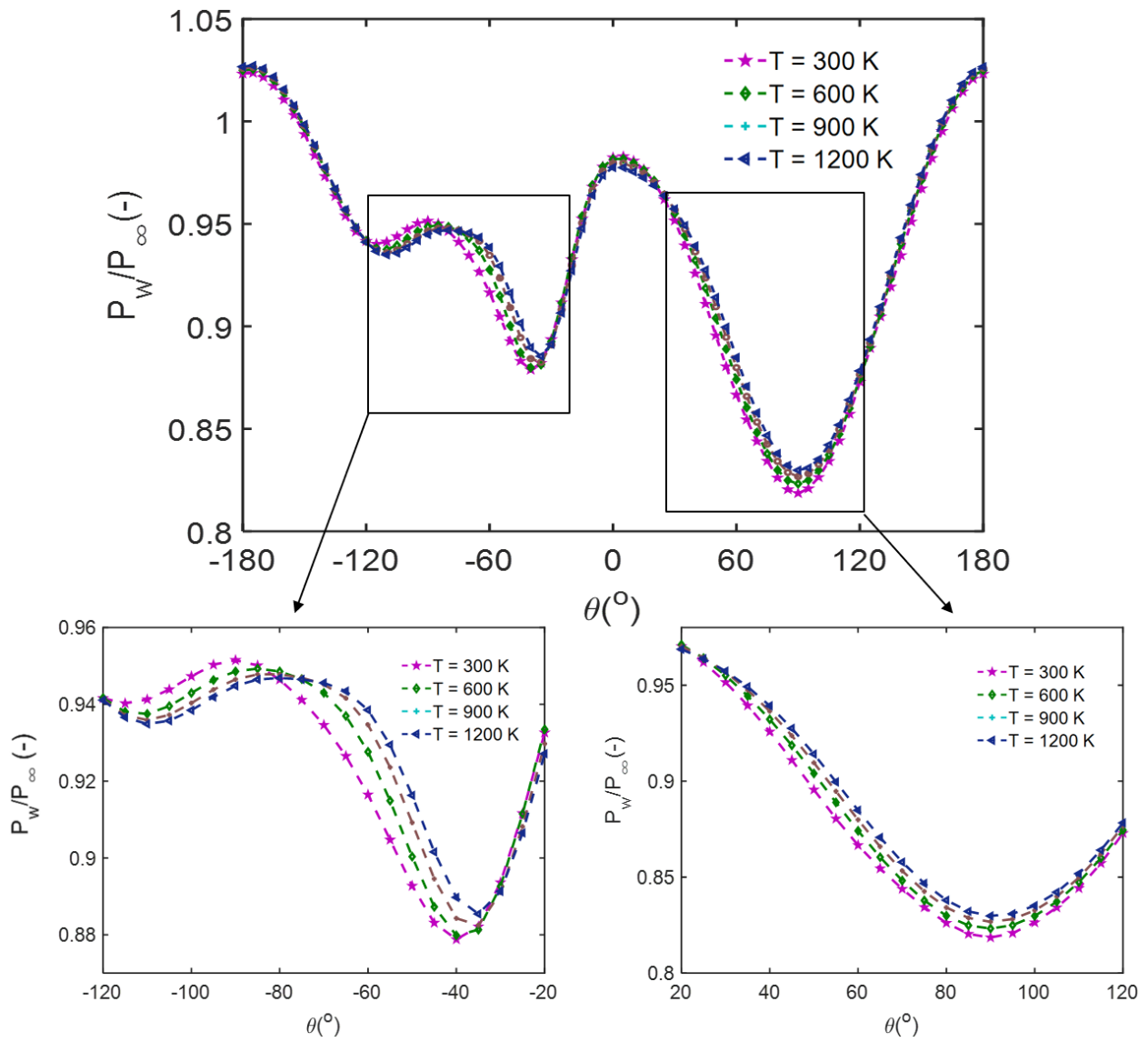


Figure 16. The effect of wall temperature on the wall pressure at $x/d = 4.5$.

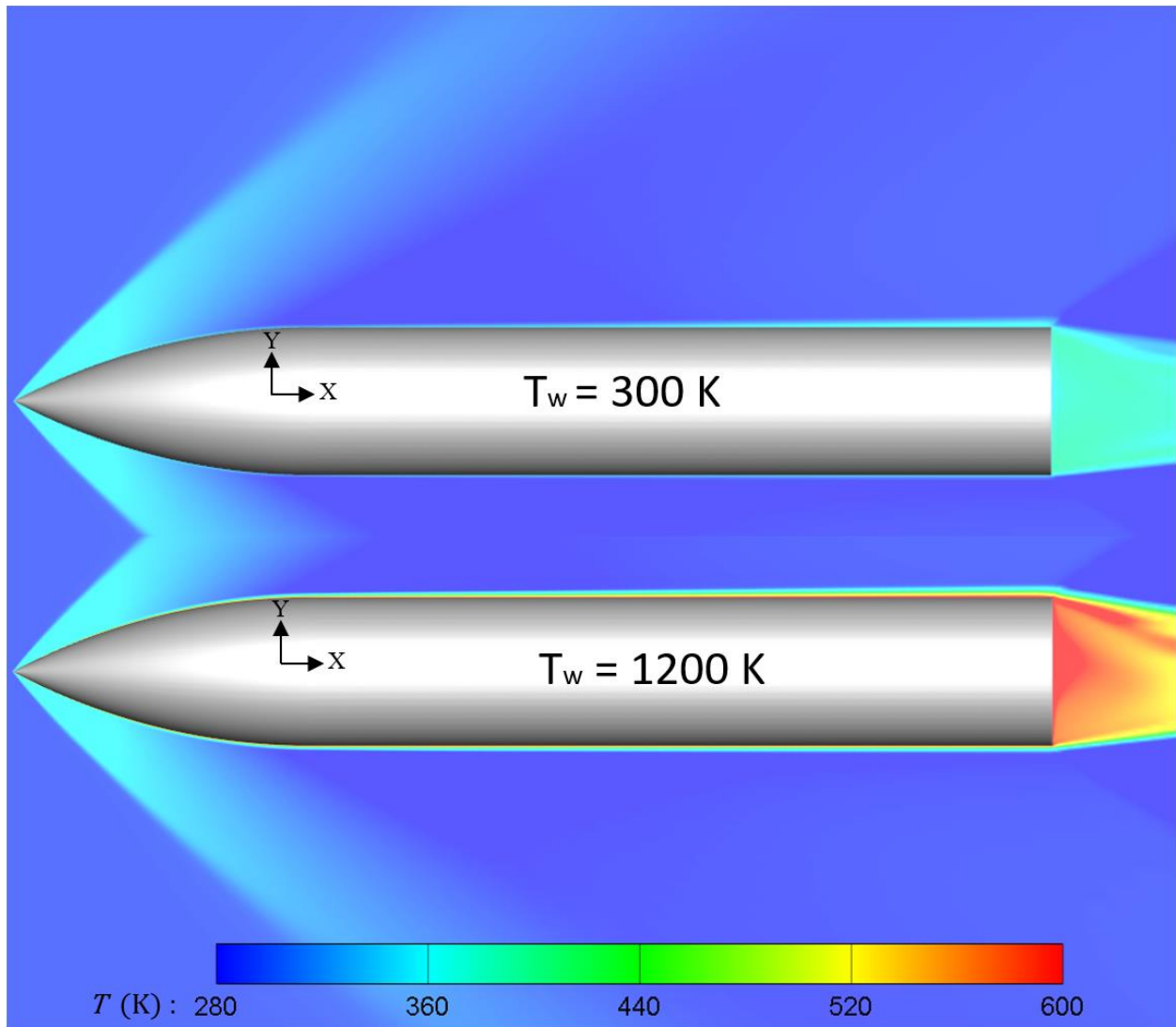
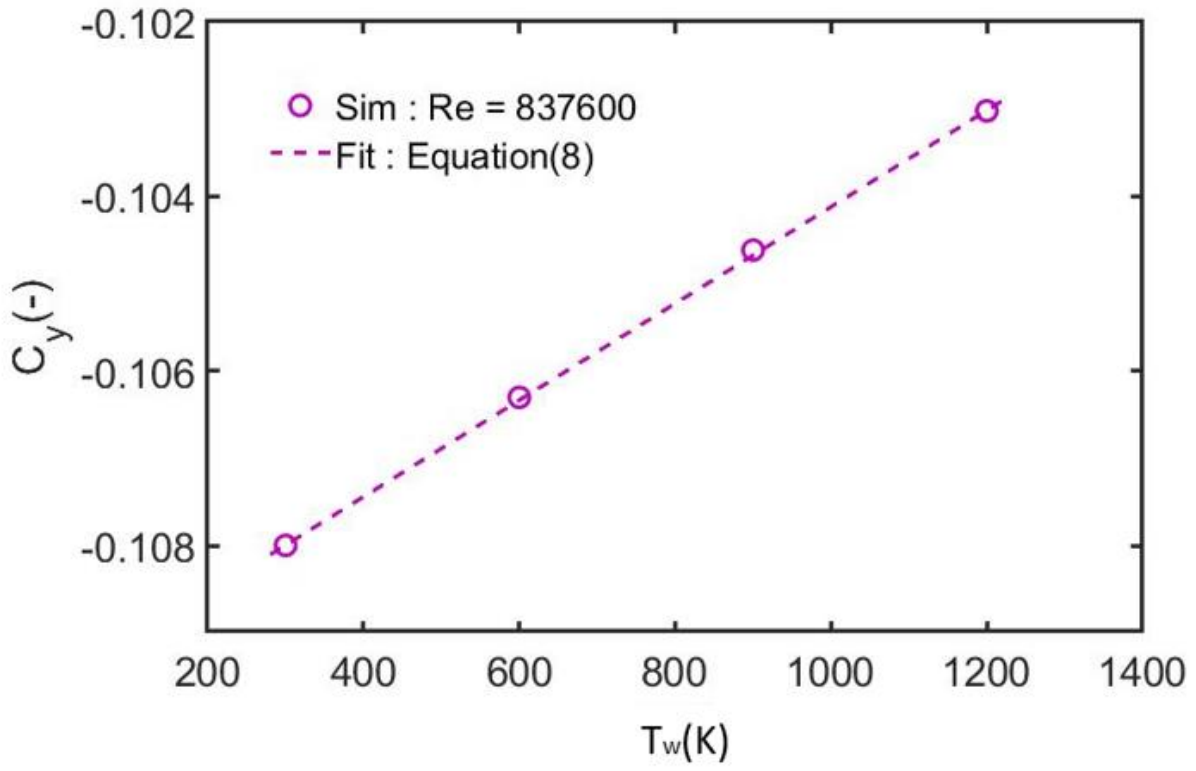
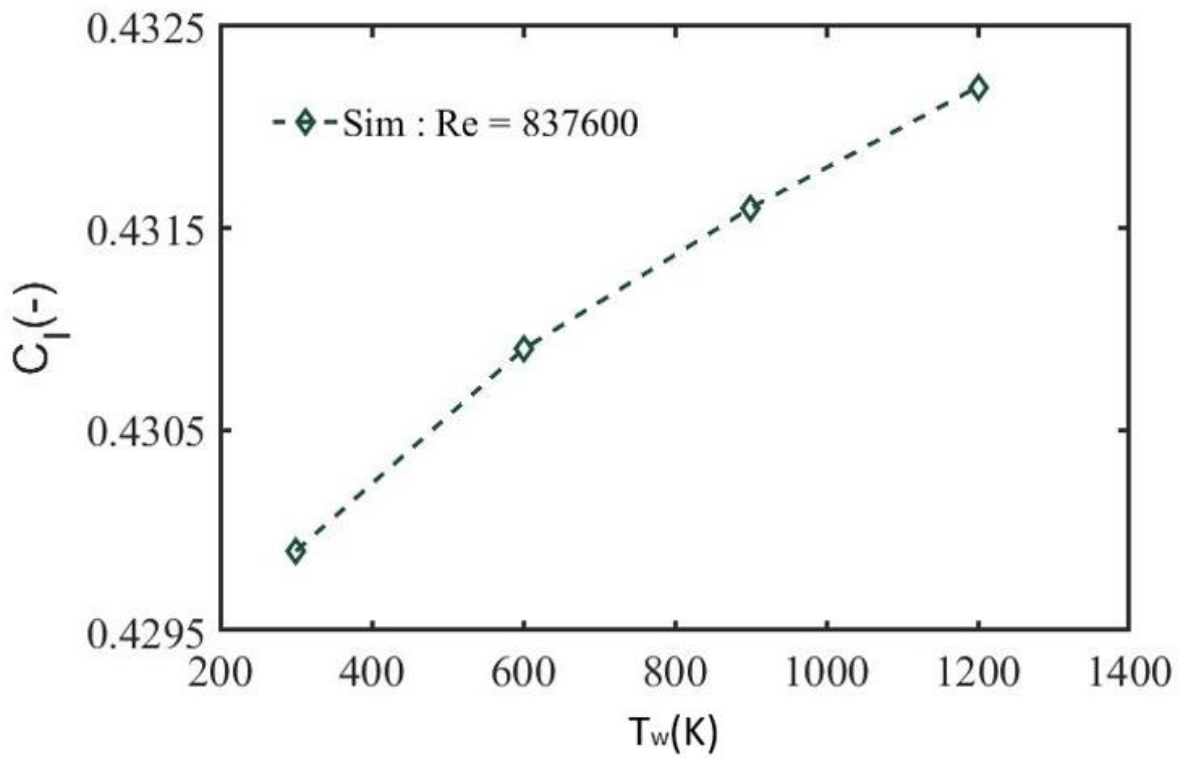


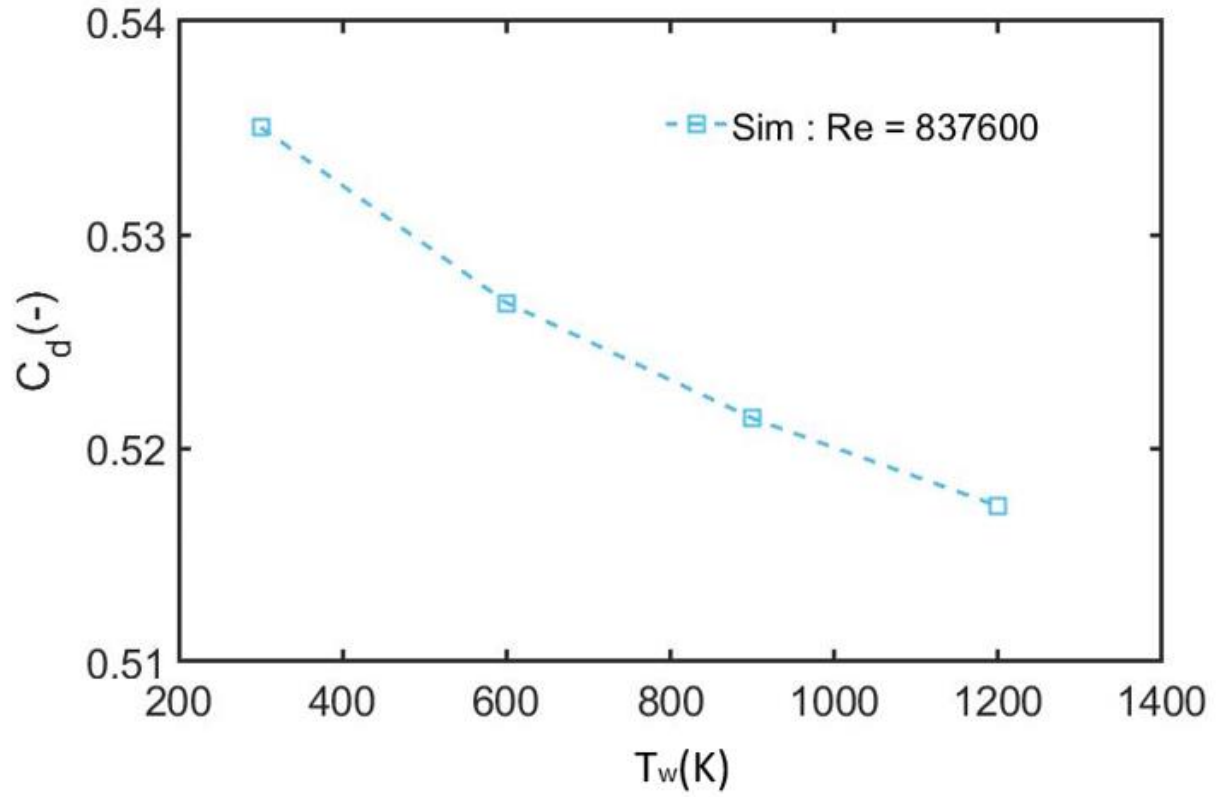
Figure 17. Temperature effect at $Ma = 1.8$, $\bar{p} = 0.315$ and $\alpha = 8$.



(a)



(b)



(c)

Figure 18. $Ma = 1.8$ and $\bar{p} = 0.315$: (a) C_{yp} ; (b) C_l ; (c) C_d against different wall temperature.

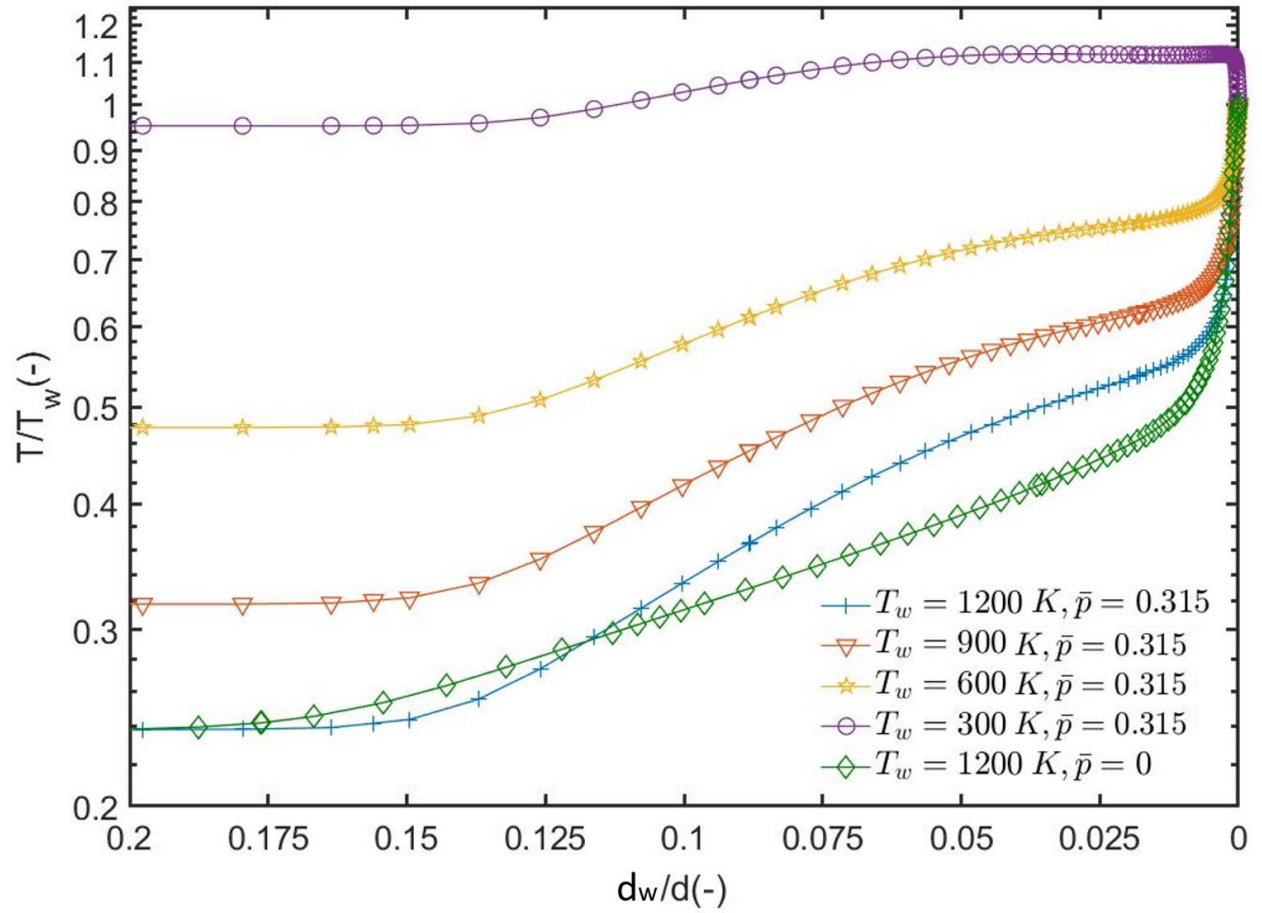


Figure 19. Wall temperature effect on the thermal boundary layer profile at $\bar{p} = 0.315$ ($\theta = -70^\circ$).

Notes on contributors



Kuiju Xue is a Ph.D. student of Beijing Institute of Technology. He received his Bachelor's degree in flight vehicle design engineering from the North University of China. Currently, he is studying at the flight control department of the School of Aerospace Engineering. His research fields are numerical simulation of complex flows and flow control. He has published three papers

in journals and conferences.



Liangyu Zhao is an Associate Professor of the School of Aerospace Engineering, Beijing Institute of Technology, Beijing, China. He received his Bachelor and Doctoral Degrees both from Beijing Institute of Technology in 2003 and 2008. His work focuses on flight vehicle design, flight dynamics and control, and aerodynamics. He has published more than 30 papers in journals

and conferences.



Qinling Li is a senior lecturer in the Department of Engineering and Mathematics, Sheffield Hallam University, UK. After receiving her Ph.D. in the School of Engineering & Science, University of Southampton, she worked as research associate on two EPSRC projects, one in Aeronautical and Automatics Engineering Department, Loughborough

University (2003 - 2006), another one in the Department of Applied Mathematics and Theoretical Physics, University of Cambridge (2006 - 2009). Her main research fields are fundamentals of

compressible turbulence, shock-waves boundary layer interaction, jet-in-cross flow & mixing enhancement, turbine/combustion chamber cooling effectiveness, fan broadband noise prediction, short take-off and vertical landing aircraft in the descending phase, high-order numerical methods used in DNS/LES, fluid-structure interaction, nanofluids and microscale fluid/heat transfer. She has published over 20 peer-reviewed publications (book/book chapters, journals and conferences).



Longyin Jiao is a Ph.D. student at Beijing Institute of Technology. He received his Bachelor's degree in engineering from the Beijing Institute of Technology. He is currently studying at the flight control department of the School of Aerospace Engineering. His research field is flow control, with two papers published in conferences.